

AD-A263 412



RL-TR-92-311
Final Technical Report
December 1992



ELECTRON TRANSPORT CALCULATIONS BETWEEN 1 MeV AND 1 eV

Arcon Corporation

Stanley Woolf



APPROVED FOR PUBLIC RELEASE; DISTRIBUTION UNLIMITED.

93 4 28 01 8

93-09041

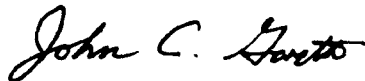


Rome Laboratory
Air Force Materiel Command
Griffiss Air Force Base, New York

This report has been reviewed by the Rome Laboratory Public Affairs Office (PA) and is releasable to the National Technical Information Service (NTIS). At NTIS it will be releasable to the general public, including foreign nations.

RL-TR-92-311 has been reviewed and is approved for publication.

APPROVED:



JOHN C. GARTH
Project Engineer

FOR THE COMMANDER



HAROLD ROTH, Director
Solid State Sciences

If your address has changed or if you wish to be removed from the Rome Laboratory mailing list, or if the addressee is no longer employed by your organization, please notify PL (VTER) Hanscom AFB MA 01731. This will assist us in maintaining a current mailing list.

Do not return copies of this report unless contractual obligations or notices on a specific document require that it be returned.

REPORT DOCUMENTATION PAGE			Form Approved OMB No. 0704-0188	
Public reporting burden for this collection of information is estimated to average 1 hour per response, including the time for reviewing instructions, searching existing data sources, gathering and maintaining the data needed, and completing and reviewing the collection of information. Send comments regarding this burden estimate or any other aspect of this collection of information, including suggestions for reducing this burden, to Washington Headquarters Services, Directorate for Information Operations and Reports, 1215 Jefferson Davis Highway, Suite 1204, Arlington, VA 22202-4302, and to the Office of Management and Budget, Paperwork Reduction Project (0704-0188), Washington, DC 20503				
1. AGENCY USE ONLY (Leave Blank)	2. REPORT DATE December 1992	3. REPORT TYPE AND DATES COVERED Final Sep 89 - Jul 92		
4. TITLE AND SUBTITLE ELECTRON TRANSPORT CALCULATIONS BETWEEN 1 MeV and 1 eV		5. FUNDING NUMBERS C - F19628-89-C-0189 PE - 61101F PR - 2306 TA - J3 WU - 37		
6. AUTHOR(S) Stanley Woolf				
7. PERFORMING ORGANIZATION NAME(S) AND ADDRESS(ES) Arcon Corporation 260 Bear Hill Road Waltham MA 02154		8. PERFORMING ORGANIZATION REPORT NUMBER N/A		
9. SPONSORING/MONITORING AGENCY NAME(S) AND ADDRESS(ES) Phillips Laboratory (PL/VTER) Hanscom AFB MA 01731-5000		10. SPONSORING/MONITORING AGENCY REPORT NUMBER RL-TR-92-311		
11. SUPPLEMENTARY NOTES Phillips Laboratory Project Engineer: John C. Garth (PL/VTER) (617) 377-2360				
12a. DISTRIBUTION/AVAILABILITY STATEMENT Approved for public release; distribution unlimited.		12b. DISTRIBUTION CODE		
13. ABSTRACT (Maximum 200 words) In this report we describe mathematical analysis, physics research and computer program development for the simulation of charged particle transport in irradiated and non-irradiated solids. The simulation techniques described were used to calculate energy deposition, charge, and current distributions in these solids. The scope of the work included: (1) discrete ordinates transport calculations of low energy (1 eV to 20 eV) electrons in silicon dioxide with and without electric fields; (2) comparison testing of one-dimensional discrete ordinates transport codes for charged and neutral particles with analytical benchmark calculations; (3) Monte Carlo transport calculations for low energy electrons in the presence of strong electric fields in silicon dioxide; (4) Monte Carlo transport calculations for high energy (MeV) electrons in insulating materials with internal electric fields.				
14. SUBJECT TERMS Discrete Ordinates, Monte Carlo Calculations, Electron Transport, Benchmark Calculations, Charge Distributions In Insulators, Electron-Phonon Interactions, Electric Fields			15. NUMBER OF PAGES 56	
			16. PRICE CODE	
17. SECURITY CLASSIFICATION OF REPORT UNCLASSIFIED	18. SECURITY CLASSIFICATION OF THIS PAGE UNCLASSIFIED	19. SECURITY CLASSIFICATION OF ABSTRACT UNCLASSIFIED	20. LIMITATION OF ABSTRACT UL	

TABLE OF CONTENTS

	Page
I. Introduction	1
II. Discrete Ordinates Electron Transport Calculations	2
1. Introduction	2
2. Low-Energy Electron Transport Calculations	2
2.1 High-Resolution(Energy) Calculations of Electron-Phonon Scatter in Silicon Dioxide	2
2.2 Discrete Ordinates Treatment of Low Energy Electron Transport in the Presence of an Electric Field	5
2.2.1 Electron Multiplication	9
2.3 Results	10
2.3.1 5eV Electron Source; Electric Field Strengths= 0 and 10^6V/cm	10
2.3.2 8eV Electron Source; Electric Field Strength= 10^6V/cm	11
2.3.3 12eV Electron Source; Electric Field Strength= $2 \times 10^6\text{V/cm}$	12
2.4 The "Continuous" Approximation Restriction	15
III. Analytical Benchmark Verification of SNCODE Algorithm	16
1. Introduction	16
2. Multigroup Benchmark Calculations	16
2.1 Results	16
2.1.1 Plane Isotropic Source; One-Group; Linearly Anisotropic Scattering	17
2.1.2 Plane Isotropic Source; Multigroup; Isotropic Scattering	18
2.1.3 Relation Between Spatial Resolution and Discretization Error	22
2.1.4 Plane Isotropic Source; Anisotropic Scattering	23
3. Analytical Benchmark Testing of One-Group SNCODE Calculations with a Material Discontinuity	27
3.1 Uniformly Distributed Source	27
3.2 Plane Isotropic Source	28
4. Analytical Benchmark Testing of One-Group SNCODE Calculations in Half-Space Geometry	29
IV. Monte Carlo Transport Calculations for Electrons in Strong Electric Fields in Silicon Dioxide	31
1. Introduction	31
2. Discussion	31
2.1 Inelastic Electron-Electron Scatter in Conducting Materials	34
V. Monte Carlo Calculations of the Transport of MeV Electrons in Insulators	37
1. Introduction	37
2. ELMC-Condensed Collision Electron Monte Carlo Code	37
3. ELMCF-Condensed Collision Electron Monte Carlo Code for Applied Electric Field Problems	42
VI. References	44

I. Introduction

During the period from September 1, 1989 through July 22, 1992, the execution of contract No. F19628-89-C-0189 was directed toward the performance of mathematical analysis, research and computer program development for the simulation and analysis of charged particle transport in irradiated and non-irradiated solids.

This report is organized into five sections in addition to this, the introduction. Section II is a discussion and presentation of research in discrete ordinates transport calculations of low energy (~ 1 -20 eV) electrons in silicon dioxide with and without applied electric fields such as are present in microelectronic devices. Section III is a brief description of research activity in the development and application of analytical benchmark calculations for one-dimensional transport in the evaluation of the accuracy of approximate discrete ordinates methods. Section IV is an account of our Monte Carlo transport calculations for low energy electrons in strong electric fields in silicon dioxide. These calculations were developed for the purpose of describing and predicting the extent and significance of the impact ionization process in microelectronic device materials. Section V presents the results of another set of Monte Carlo electron transport calculations which we developed for describing the transport of MeV electrons in insulating materials with internal, polarization-induced electric fields. Section VI, the final section, is the reference list.

DISC (11/11/92)

Accession For	
NTIS GRA&I	<input checked="" type="checkbox"/>
DTIC TAB	<input type="checkbox"/>
Unannounced	<input type="checkbox"/>
Justification	
Distribution/	
Availability Codes	
Avail and/or	
Dist	Special
A-1	

II. Discrete Ordinates Electron Transport Calculations

1. Introduction

In earlier research efforts involving the method of discrete ordinates (S_N) for the solution of electron transport problems, we had made extensive use of the transport code ONETRAN^[1], as reported in Ref. 2. As the research activity continued, however, it became clear that creation of a new computer program with the ONETRAN linear discontinuous and diamond differencing algorithms would be highly useful. It was our intention to apply the S_N method to a variety of electron transport problems covering a wide range of electron energies and scattering processes, from the eV range in which electron-phonon scattering is important to the MeV range in which the Mott scattering model is applicable. It became apparent to us that if the S_N method were to be effectively applied to electron-phonon scattering in microelectronic device materials, it would be necessary to build into the S_N program a capability for inclusion of applied electric field effects, since the voltages typically applied to silicon devices produce large internal electric fields. Algorithm modifications such as this would be difficult, if not impossible, to accomplish with the ONETRAN code without encountering serious problems that could arise from programming error and/or algorithm incompatibility.

The applicability of SNCODE is restricted to slab geometry. The sacrifice in generality has resulted in a program that is simpler than ONETRAN, which treats cylindrical and spherical geometries as well. Another departure from the ONETRAN method is that SNCODE computes, preserves and uses the angular components of the flux, while ONETRAN does the same with the Legendre series expansion coefficients of the angular flux. The actual angular components are computed for the spatial differencing procedure and then discarded. The ONETRAN method is more computationally efficient when the scattering cross sections are given in terms of their Legendre expansion coefficients, which is usually the case. While the two methods are equivalent, it is not convenient to apply the ONETRAN approach when dealing with applied electric fields oriented along a single direction. In the following sections we will discuss various applications of SNCODE to : 1) electron-phonon scattering with and without applied electric fields; and 2) benchmark calculations and verification of differencing algorithm accuracy.

2. Low-Energy Electron Transport Calculations

2.1 High-Resolution (Energy) Calculations of Electron-Phonon Scatter in Silicon Dioxide

The discrete ordinates transport method was used to calculate electron energy spectra resulting from electron-phonon scatter in SiO_2 under zero electric field conditions. SNCODE was installed and run on the Phillips Laboratory CRAY-2. The availability of the supercomputer provided an opportunity to make very high resolution calculations of these electron energy spectra. A cross section set was generated for 2000 energy groups of uniform width over the interval 0-10 eV ($\Delta E = 0.005$ eV). This allowed full recognition of the discrete optical mode energy transitions (.068, .153 eV) and a reasonably accurate representation of the smaller acoustic mode energy changes (maximum energy transfer ~ 0.02 eV). A 5 eV electron source was positioned at the center plane of a SiO_2 slab of thickness 100 nm. The source was directed to the right side of the center plane with a cosine-squared (μ^2 ; see insets of Figs. 1 and 2) angular distribution. The 2000 group run was made using an energy group in-scatter source

error tolerance of $\epsilon_g = 10^{-3}$. That is, a number of outer (energy) iterations were made until the group with largest error in in-scatter source reached a value $\leq \epsilon_g$. For this case, the required number of outer iterations was 29. The highest energy group containing up-scattered electrons (in-scatter source $\sim 10^{-8}$), given the above convergence condition, was group 883, corresponding to ~ 5.6 eV. The resulting energy spectra show the optical mode transition lines at the low energy end superimposed on

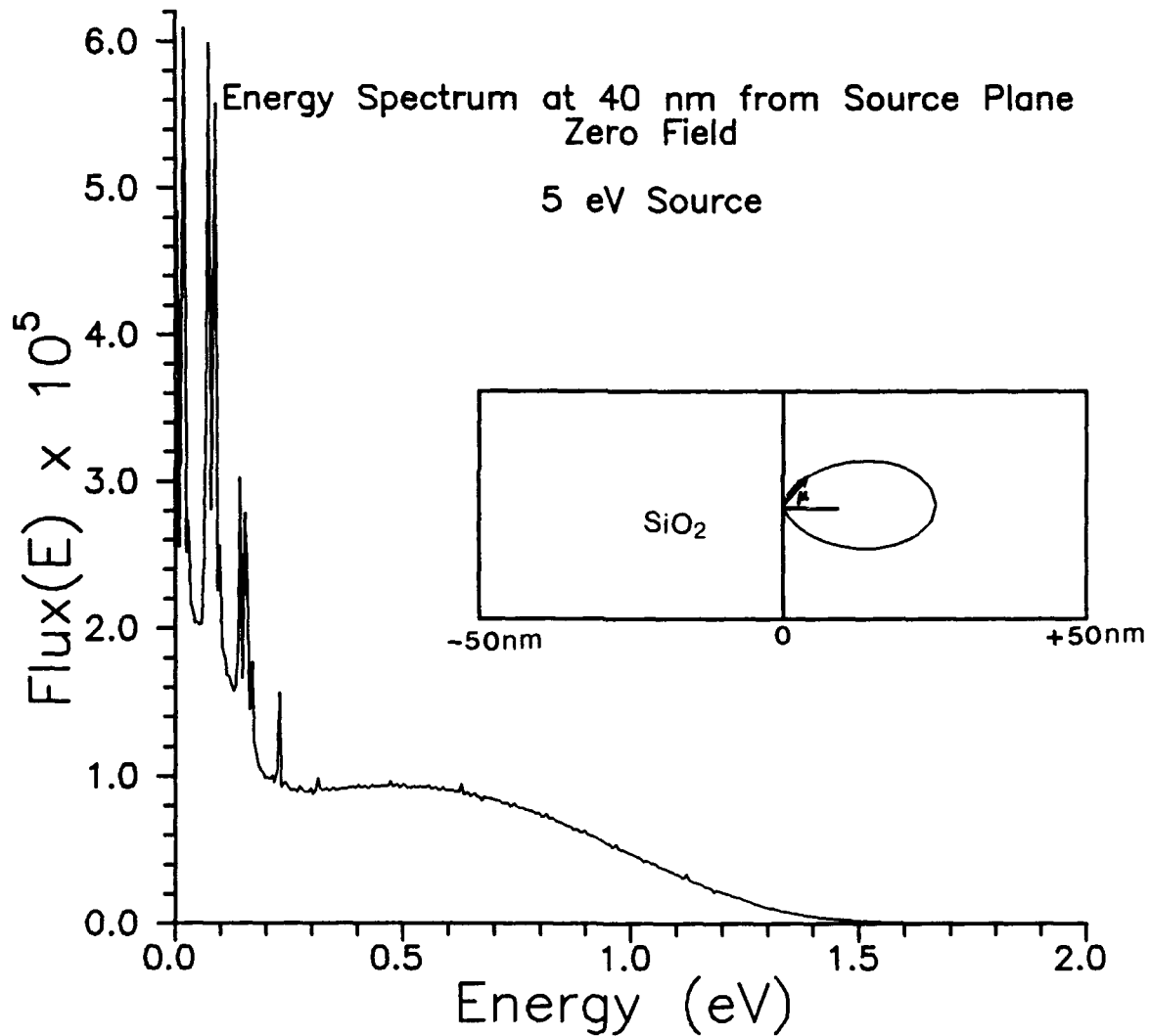


Fig. 1. Electron energy spectrum at +40 nm in SiO₂ under zero field conditions. Electron source, 5 eV, located at center plane of 100nm slab is μ^2 distributed, directed to the right of center plane. Spectrum structure results from electron-phonon interactions.

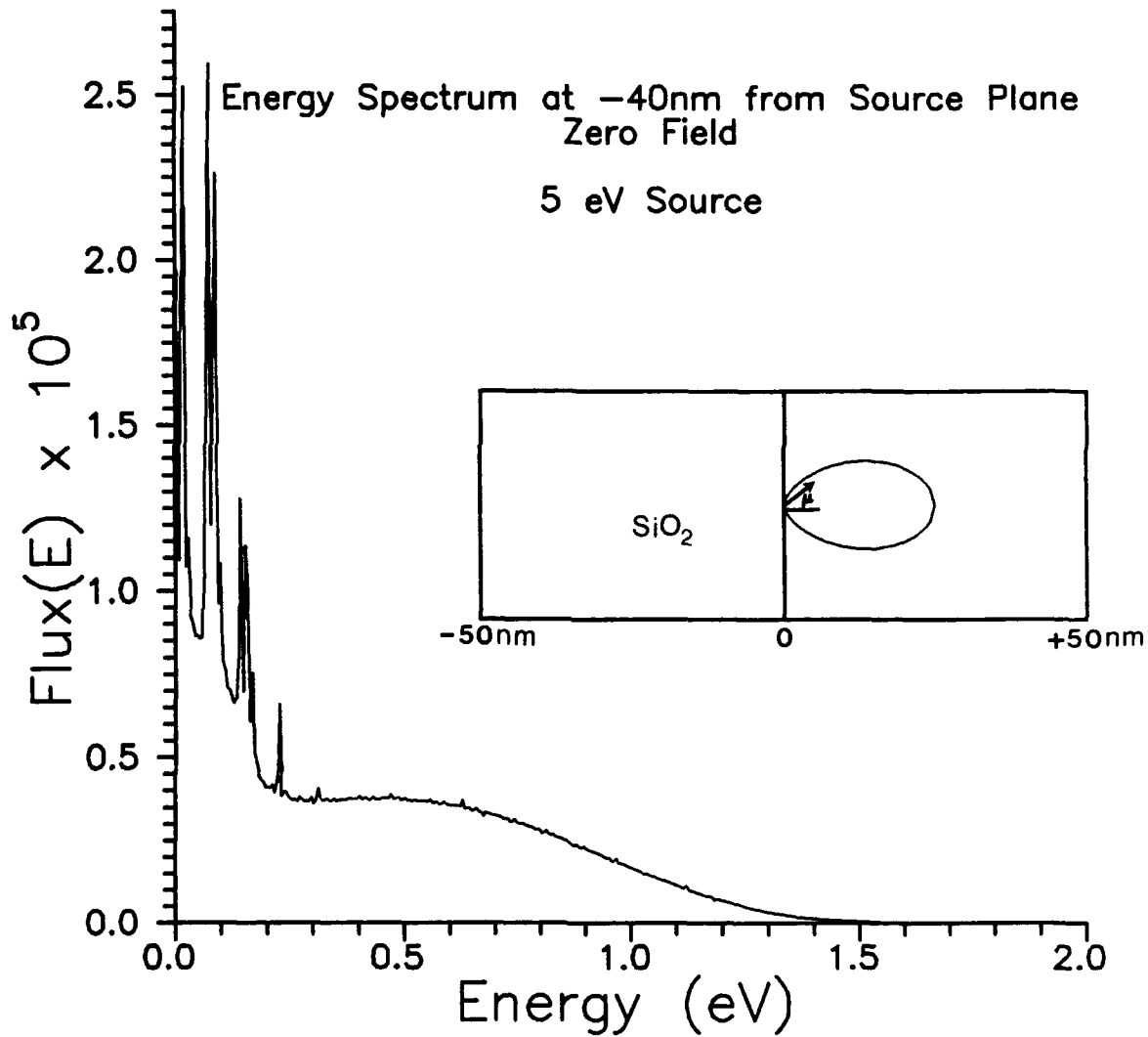


Fig. 2. Electron energy spectrum at -40 nm in SiO_2 under zero field conditions. Electron source, 5 eV, located at center plane of 100nm slab is μ^2 distributed, directed to the right of center plane. Spectrum structure results from electron-phonon interactions.

the largely acoustic mode generated smooth spectrum. As evidenced by the spectra shown in Figs. 1 and 2, the S_N method provided a degree of energy spectrum resolution not obtainable with the Monte Carlo method. The two spectra, shown at $+40$ nm (Fig. 1) and -40 nm (Fig. 2), are similar. The amount of electron scattering at these distances is sufficient to nearly eradicate any differences due to source directionality. The spacing of the peaks is consistent with the values of the optical mode energy transitions given above.

2.2 Discrete Ordinates Treatment of Low Energy Electron Transport in the Presence of an Electric Field

Modifications were made to the S_N program, SNCODE, to account for the effects of the presence of an electric field on electron transport in solids. The objective of this effort was to model low energy electron transport, electron-phonon scattering, and production of secondary electrons due to impact ionization, in the oxide layer of a silicon device under typical operating conditions, i.e. applied voltage ≈ 5 V. Much of our method for the treatment of electric field effects was based on the earlier formulation of Wienke^[3] in which he incorporated a Lorentz force term into the Boltzmann equation (no-relativistic) for electrons.

The multigroup non-relativistic Boltzmann transport equation (in one-dimension) for group g electrons in the presence of an electric field is

$$\mu \frac{\partial \phi_g}{\partial x} + \sigma_T^g \phi_g(x, \mu) + \frac{e}{m_0 v_g} \vec{\mathcal{E}} \cdot \nabla_v \phi_g(x, \mu) = Q_{fg} + Q_{sg} \quad (1)$$

where

$\phi_g(x, \mu)$ is the group g flux,

x and μ are the position and velocity direction cosine, defined in the usual way,

σ_T^g is the total cross section,

$\vec{\mathcal{E}}$ is the electric field strength,

e is the electronic charge,

m_0 is the electron rest mass,

v_g is the velocity of group g electrons,

Q_{fg} is the fixed source for group g ,

and Q_{sg} is the in-scatter source to group g .

Our approach differed from that of Wienke in that we began with the Boltzmann equation rather than the Fokker-Planck equation. SNCODE is a Boltzmann solver and, as will be demonstrated elsewhere in this document, operates correctly for applications in which no electric field is present. We treated the velocity gradient electric field term in the same manner as Wienke.

Since our multigroup discrete ordinates equation solves for the flux as a function of energy, i.e. $\phi_g(x, \mu) \approx \phi(x, \mu, E_g)$, it was necessary to re-express the velocity gradient term in terms of the energy variable. The electric field $\vec{\mathcal{E}}$ was assumed to be directed along \vec{r} . With the electron velocity given by \vec{v} , and the velocity direction cosine with respect to the field direction given by μ (see Fig. 3),

$$\mu = \frac{\vec{r} \cdot \vec{v}}{rv} \quad (2)$$

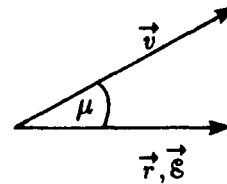


Fig. 3. Vector diagram showing relative orientations of electric field and electron motion.

The following useful identity for the velocity gradient operator is given in Ref. 3 as

$$\nabla_v = \frac{\vec{v}}{v} \frac{\partial}{\partial v} + \left(\frac{\vec{r}}{rv} - \frac{\mu \vec{v}}{v^2} \right) \frac{\partial}{\partial \mu} . \quad (3)$$

Defining

$$\mathcal{L} \equiv \frac{e}{m_0 v} \vec{s} \cdot \frac{\vec{v}}{v} \frac{\partial}{\partial v} \quad \text{and} \quad \mathcal{M} \equiv \frac{e}{m_0 v} \vec{s} \cdot \left(\frac{\vec{r}}{rv} - \frac{\mu \vec{v}}{v^2} \right) \frac{\partial}{\partial \mu} , \quad (4)$$

then

$$\frac{e}{m_0 v} \vec{s} \cdot \nabla_v = \mathcal{L} + \mathcal{M} . \quad (5)$$

The procedure for incorporation of the velocity derivative term \mathcal{L} into the multigroup Boltzmann will be outlined first, and that for the angular derivative term \mathcal{M} will be given second.

The operator \mathcal{L} can be simplified as follows:

$$\begin{aligned} \mathcal{L}\phi &= \frac{e}{m_0 v} \vec{s} \cdot \frac{\vec{v}}{v} \frac{\partial \phi}{\partial v} \\ &= \frac{e}{m_0 v} \vec{s} \cdot \frac{\vec{r}}{r} \cdot \frac{\vec{v}}{v} \frac{\partial \phi}{\partial v} \\ &= \frac{e\mu}{m_0 v} \vec{s} \cdot \frac{\partial \phi}{\partial v} . \end{aligned} \quad (6)$$

Our multigroup- S_N calculation requires that the flux be expressed in terms of energy rather than velocity. For non-relativistic calculations, the velocity derivative can be directly expressed in terms of energy derivatives.

$$\frac{\partial}{\partial v} = \frac{dE}{dv} \frac{\partial}{\partial E} \quad \text{and} \quad E = \frac{1}{2} m_0 v^2, \quad (7)$$

$$\text{thus} \quad \frac{\partial}{\partial v} = m_0 v \frac{\partial}{\partial E} \quad (8)$$

and

$$\mathcal{L}\phi = e\vec{s} \cdot \mu \frac{\partial \phi}{\partial E} . \quad (9)$$

Eqn. (1) can then be restated as

$$\mu \frac{\partial \phi_g}{\partial x} + \sigma_T^g \phi_g(x, \mu) + [e\vec{s} \cdot \mu \frac{\partial}{\partial E} + \mathcal{M}] \phi_g(x, \mu) = Q_{fg} + Q_{sg} . \quad (10)$$

In finite difference terms, the energy derivative term becomes

$$\mathcal{L} \approx e\vec{s} \cdot \mu \frac{\phi_g - \phi_{g+1}}{E_g - E_{g+1}} \quad \text{for } \mu > 0, \quad (11a)$$

$$\mathcal{L} \approx e\vec{s} \cdot \mu \frac{\phi_g - \phi_{g-1}}{E_g - E_{g-1}} \quad \text{for } \mu < 0 . \quad (11b)$$

The $\mu > 0$ case corresponds to energy upscatter by the field, and the $\mu < 0$ case corresponds to energy downscatter. In the former, the positive velocity direction cosine indicates that the electron is moving with the field direction, while in the latter, the electron motion is in opposition to the field direction. If we order the energy groups such that $E_{g-1} > E_g > E_{g+1}$, and designate the energy group width at E_g as ΔE_g , then the field acceleration terms become

$$L \approx e\mathcal{E}\mu \frac{\phi_g - \phi_{g-1}}{\Delta E_g} + 1 \quad \text{for } \mu > 0, \quad (11a)$$

$$L \approx -e\mathcal{E}\mu \frac{\phi_g - \phi_{g-1}}{\Delta E_g} \quad \text{for } \mu < 0. \quad (11b)$$

The finite difference (in the energy variable) form of Eq. 10 then becomes

$$\mu \frac{\partial \phi_g}{\partial x} + \sigma_T^g \phi_g(x, \mu) + \left[\frac{e\mathcal{E}\mu}{\Delta E_g} + \mathcal{M} \right] \phi_g(x, \mu) = \frac{e\mathcal{E}\mu}{\Delta E_g} \phi_{g+1} + Q_{fg} + Q_{sg} \quad (\mu > 0), \quad (12a)$$

$$\mu \frac{\partial \phi_g}{\partial x} + \sigma_T^g \phi_g(x, \mu) + \left[-\frac{e\mathcal{E}\mu}{\Delta E_g} + \mathcal{M} \right] \phi_g(x, \mu) = -\frac{e\mathcal{E}\mu}{\Delta E_g} \phi_{g-1} + Q_{fg} + Q_{sg} \quad (\mu < 0). \quad (12b)$$

In Eqs. 12a,b the terms involving $\phi_{g\pm 1}$ have been transposed to the right-hand (source) side and can be regarded as positive, angularly dependent contributions to the in-scatter source. The $e\mathcal{E}\mu/\Delta E_g$ term on the left side has the effect of adding a positive angularly-dependent term to the total cross section.

The angular derivative term,

$$\mathcal{M} = \frac{e}{m_0 v} \vec{\mathcal{E}} \cdot \left(\frac{\vec{r}}{rv} - \frac{\mu \vec{v}}{v^2} \right) \frac{\partial}{\partial \mu}, \quad (4)$$

can be written as^[3]

$$\mathcal{M} = \frac{e}{m_0 v^2} \mathcal{E} (1 - \mu^2) \frac{\partial}{\partial \mu}, \quad (13)$$

which has the same form as the angular part of the Fokker-Planck operator and represents a within-group angular redistribution (trajectory bending) by the electric field. Because electron-phonon interactions are largely characterized by wide angle scatters, the extended P_{12} transport correction adequately handles the scattering angular distribution. After a small number of scatters, the flux is not highly anisotropic, and the angle derivative can be evaluated with a flux Legendre expansion of order 12; assuming that

$$\phi_g(\mu) \approx \sum_{l=0}^{12} \left(l + \frac{1}{2} \right) \phi_g^l P_l(\mu) \quad (14)$$

then making use of the identity

$$(1 - \mu^2) \frac{\partial P_l}{\partial \mu} = \frac{l(l+1)}{2l+1} (P_{l-1}(\mu) - P_{l+1}(\mu)),$$

yields

$$(1 - \mu^2) \frac{\partial \phi_g}{\partial \mu} \approx \sum_{l=0}^{12} \frac{l(l+1)}{2} \phi_g^l (P_{l-1}(\mu) - P_{l+1}(\mu)), \quad (15)$$

where the flux moments ϕ_g^l are obtained with well-known expression

$$\phi_g^l = \int_{-1}^{+1} d\mu \phi_g(\mu) P_l(\mu).$$

With the above expression for \mathcal{M} , the Boltzmann equation is then given by

$$\mu \frac{\partial \phi_g}{\partial x} + \left[\sigma_T^g \pm \frac{e\mathcal{E}\mu}{\Delta E_g} + \frac{e\mathcal{E}}{2E_g} (1 - \mu^2) \frac{\partial}{\partial \mu} \right] \phi_g = \pm \frac{e\mathcal{E}\mu}{\Delta E_g} \phi_{g\pm 1} + Q_{fg} + Q_{sg} \quad (\mu > 0), \quad (16)$$

where the \pm denotes $+$ for $\mu > 0$ and $-$ for $\mu < 0$.

In the above, it is assumed that energy transfers due to electric fields occur between adjacent groups, the continuous approximation (CDSA). Eq. 16, the multigroup transport equation, is solved in the usual manner by the method of discrete ordinates. The spatial differencing scheme used is linear-discontinuous, and the discrete ordinate angles are chosen as Gauss quadrature ordinates.

The formulation given above was implemented in SNCODE, and the results were reported in Ref. 4. In this work, the cross section parameters for the multigroup calculations were derived from the inverse mean free path and stopping power expressions of Ashley^[5,6]. The width structure of the energy groups was chosen in order to make use of averaged quantities (cross section, stopping power). As illustrated in the graph of Fig. 4, the stopping power, averaged over all individual electron-phonon interaction modes, is negative. Thus in the Q_{sg} term of Eq. 16 above, the group transfer cross sections for electron-phonon interactions, $\sigma_g^{ep \rightarrow g}$ in Eq. 17 below, were characterized only by downscatter.

$$\sigma_g^{ep \rightarrow g} = \sigma_{g-1 \rightarrow g}^{ep} = \frac{|\langle \frac{dE}{ds} \rangle_{6 \text{ modes}}|}{\Delta E_g} \quad (17)$$

Up-scatter can only occur via electric field action.

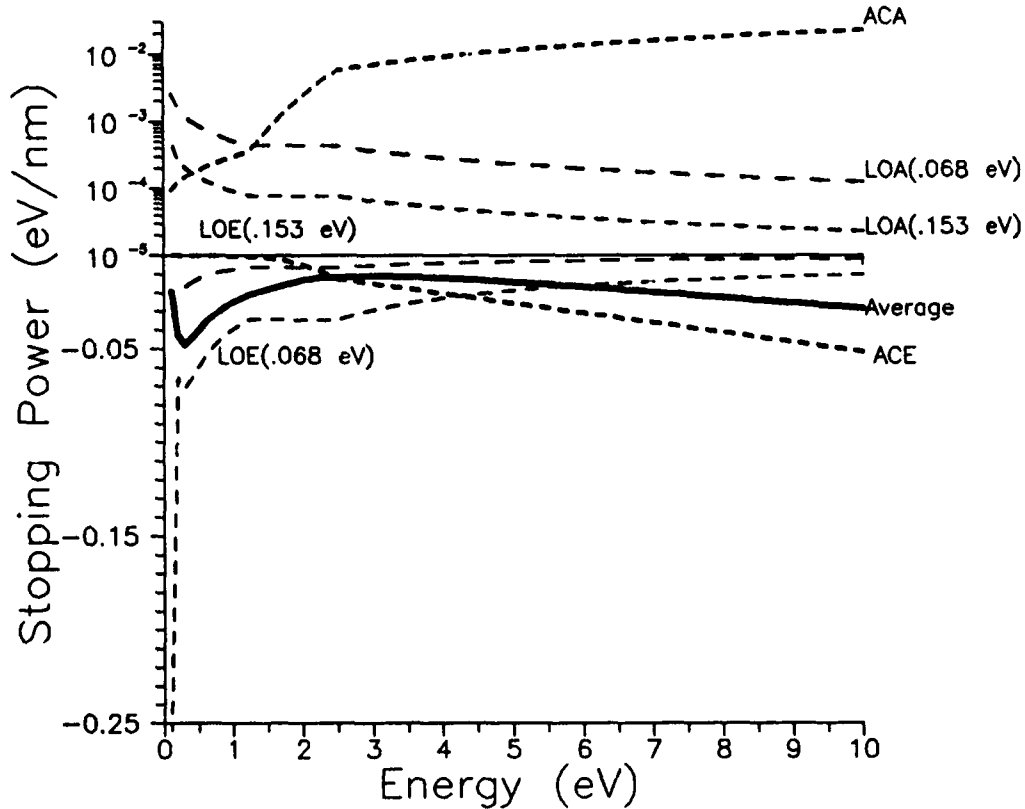


Fig. 4. Individual mode and averaged electron stopping powers for electron-phonon interactions in SiO_2 .

2.2.1 Electron Multiplication

To account for the secondary electron production which can occur through impact ionization in SiO_2 when the primary electron energy exceeds 8.9eV, we utilized a set of ionization cross sections calculated from the theory, developed by Ritchie^[7] and Ashley^[8]. In our S_N calculations, impact ionization was treated as $(e, 2e')$ scattering. The energies of the primary and secondary electrons after the ionizing collision were assumed equal and were given as follows:

$$E_f = \frac{1}{4} (E_i - E_{gap}), \quad (18)$$

where E_i = initial energy of primary electron,
and E_f = final energy of primary electron,
= energy of secondary electron.

The factor of 1/4, rather than 1/2 arose from the allocation of an equal amount of recoil energy to holes. Figure 5 is a plot of the ionization cross section, shown together for comparison purposes, with the phonon scatter cross section. It is seen that at 10eV, the ionization component is lower than the phonon scatter by more than two orders of magnitude. However, in the 12-14eV range, this factor is narrowed to approximately 15. Thus, at sufficiently high energies, significant impact ionization is possible.

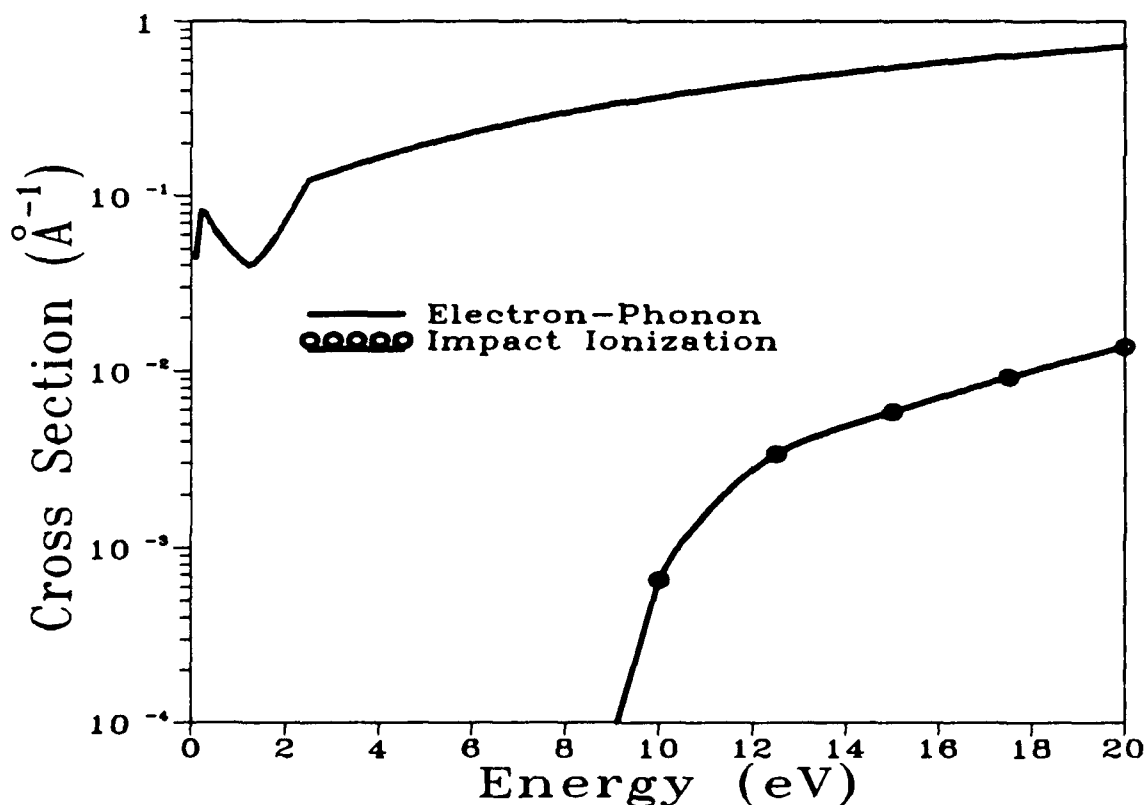


Fig. 5. Comparison plot of electron-phonon interaction and impact ionization cross sections in SiO_2 .

2.3 Results

2.3.1 5eV Electron Source; Electric Field Strengths = 0 and 10^6 V/cm

S_4 calculations were made with SNCODE for a 5eV isotropic source of electrons, uniformly distributed over the interval 40-60 nm in the SiO_2 slab (thickness = $0.1 \mu\text{m}$) as shown in Fig. 6. A uniform electric field of strength $\mathcal{E}_z = 10^6$ V/cm was assumed oriented along the z-direction. The energy group structure consisted of 100 uniformly spaced groups of width $\Delta E_g = 0.1$ eV spanning the energy range 0-10 eV. The spatial discretization was chosen so that a change in the electron position of one Δz interval would not produce a field-induced change in the electron energy of more than one ΔE_g . This is an essential requirement for these calculations, since it is assumed that energy transfers due to the electric field are allowed to occur only between adjacent groups, the "continuous approximation"^[2]. In order to maintain a consistent set of discretization parameters in these S_N calculations, either the spatial resolution or the energy group width (or both) must also be increased as the value of \mathcal{E}_z is increased.

Fig. 6 shows a set of spatial flux profiles at 8 energies (1, 2, 3, 3.5, 4, 4.5, 5, 5.5 eV), for $\mathcal{E}_z = 10^6$ V/cm. The flux curves shifted in the direction of \mathcal{E}_z , and the field-induced up-scatter is evidenced by the presence of flux curves at energies in excess of 5 eV.

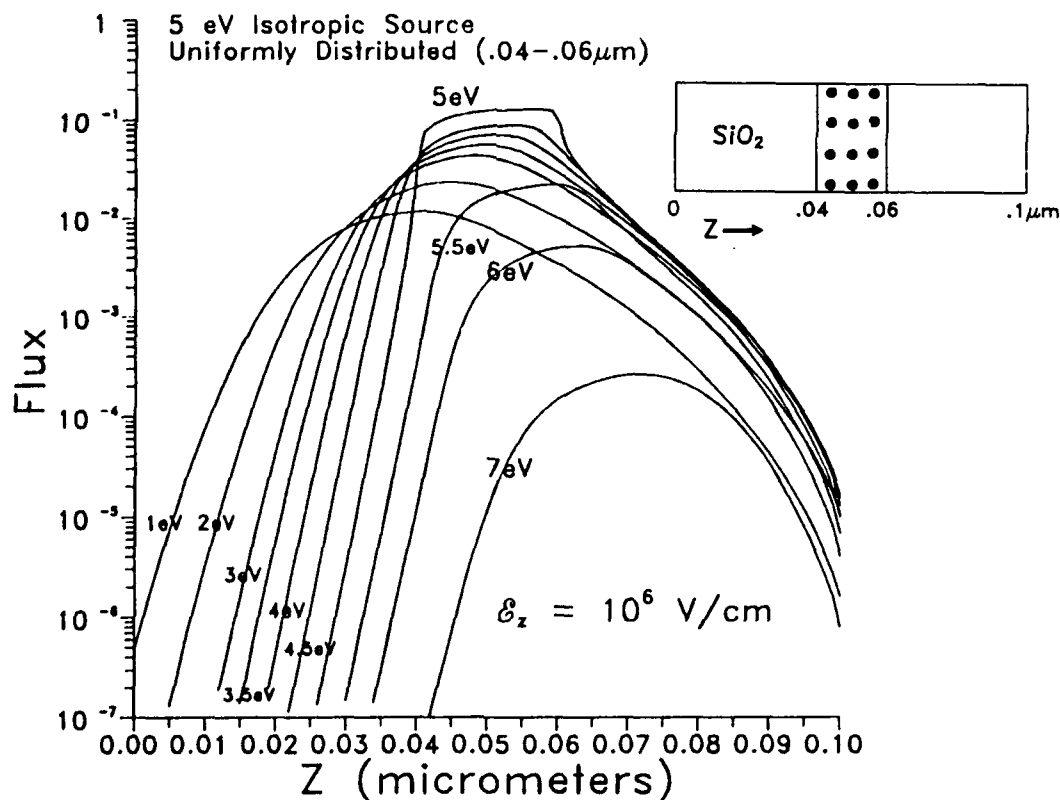


Fig. 6. Electron flux profiles at 10 energies with electric field ($\mathcal{E}_z = 10^6$ V/cm). Uniformly distributed (.04-.06 μm), 5 eV isotropic electron source in SiO_2 ^[4].

The effect of the electric field on the distribution of electron energies is also shown in Fig. 7 where the respective energy spectra for $\mathcal{E}_z = 0$ and $\mathcal{E}_z = 10^6 \text{ V/cm}$ are plotted at $z = .09 \mu\text{m}$, where the spectra have stabilized. As can be seen, the results predict that a field value of $\mathcal{E}_z = 10^6 \text{ V/cm}$ is nearly sufficient to promote the electron energy above the 8.9 eV ionization threshold.

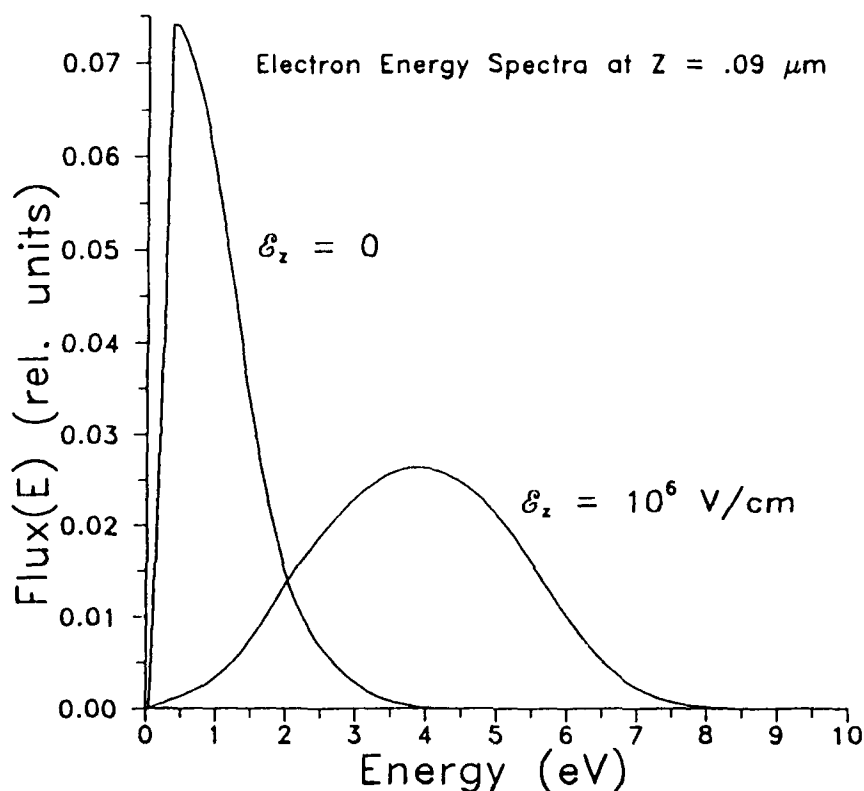


Fig. 7. Electron energy spectra for uniformly distributed (.04-.06 μm) 5 eV isotropic electron source in SiO_2 with $\mathcal{E}_z=0$ and $\mathcal{E}_z=10^6 \text{ V/cm}$.^[4]

2.3.2 8eV Electron Source; Electric Field Strength = 10^6 V/cm .

With the same geometry as shown in the Fig. 6 inset, the electron source energy was increased to 8eV, a value slightly below the ionization threshold. From this starting point, electron acceleration due to the 10^6 V/cm . field, in combination with the positive contribution of the phonon absorption terms to the electron-phonon interaction stopping power, were sufficient to promote the source electrons to energies in excess of E_{gap} . The S_N calculation was performed using 140 uniformly spaced energy groups ($\Delta E = 0.1 \text{ eV}$), 100 uniform spatial steps ($\Delta z = .001 \mu\text{m}$), and as in the previous case, 4 discrete ordinates. With the outer iteration convergence precision of 10^{-2} , it was found that 15 outer iterations were required for convergence.

Figures 8a and 8b show the electron energy flux spectra as a function of distance from the left and right edges, respectively, of the source band. These spectra are not absolute. That is, at each value of z , the flux profile as a function of energy is shown. Thus, while the low energy peak ($\sim 0.4\text{eV}$) in Fig. 8a, for example, appears larger than the peak at $\sim 8\text{eV}$, the opposite is actually true in absolute terms, as would be expected from inspection of the cross section curves of Fig. 5. We concluded that the low energy peak in Fig. 8a was primarily due to downscatter (phonon emission) and deceleration caused by the electric field. The 0.4eV peak occurs at a distance $0.04\text{ }\mu\text{m}$ from the source band. During the transport, these initially back-directed electrons travel in opposition to the field direction; their mean free path increases as they lose energy; and their direction of travel remains "locked-in" to the negative direction. The electric field alone accounted for a 4eV energy loss over the $.04\text{ }\mu\text{m}$ distance. On the right side of the source region (Fig. 8b) there is a sharp peak at the 8eV source energy, with a high energy tail extending to $\sim 9.9\text{eV}$. Clearly here, energy downscatter still dominates, but the energy loss rate is moderated by acceleration due to the field, so that the peak declines gradually. The low energy peak at $.04\text{ }\mu\text{m}$ occurs at 1.8eV . This may be attributable in part to acceleration by the field of both downscattered electrons and secondary electrons arising from the promotion of the 8eV source electrons to energies exceeding E_{gap} .

2.3.3 12eV Electron Source; Electric Field Strength = $2 \times 10^6\text{ V/cm}$.

Another 140 group S_N calculation was performed for a 12eV source with $E_f = 2 \times 10^6\text{ V/cm}$. for the same problem geometry as above. To preserve the applicability of the "continuous approximation" with regard to energy gain/loss due to the field, the resolution of the spatial discretization mesh was doubled ($\Delta x = .0005\text{ }\mu\text{m}$) beyond that used in the previous case. This calculation converged with fewer outer iterations (12) than were required for the 10^6 V/cm . case (15). Three possible reasons for this are: 1) fewer up-scatter (phonon absorption events) were required in this calculation to reach the 14eV upper bound due to the higher source energy in this calculation, 12eV rather than 8eV ; 2) also because of the higher source energy, secondary electron production began with the first outer iteration; and 3) the doubling of the electric field force resulted in a more rapid promotion of the 12eV electrons to higher energies.

The doubling of the electric field strength, in combination with the increased source energy, results in an enhancement of low energy secondary electron production. Figure 9a is a plot of the electron energy spectra vs. distance from the left side of the source. Unlike the 10^6 V/cm . case shown in Fig. 8a, there is a small peak of low energy electrons adjacent to the source region. These are secondary electrons which, when produced, can range in energy from 0.75 to 1.5eV . Similarly, in Fig. 9b, the spectra on the right side of the source, a low energy peak near the source region appears, also in contrast with the previous case. The electric field strength of $2 \times 10^6\text{ V/cm}$. was insufficient to overcome the phonon emission downscatter; thus the secondary electron energy remained low.

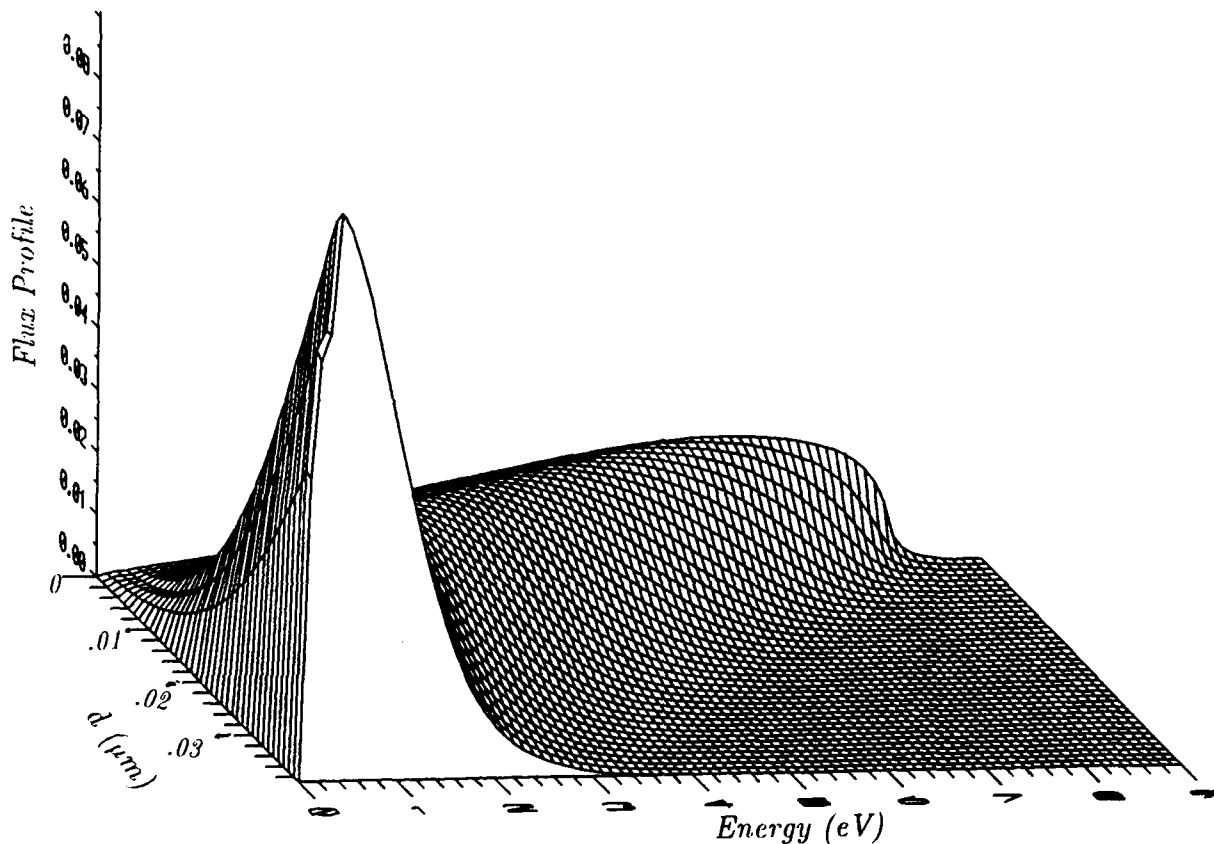


Fig. 8a. Electron energy flux spectrum profiles vs. distance, $d(\mu\text{m})$, from left edge of source region in SiO_2 (Fig.6 inset). Source energy = 8eV. $\mathcal{E}_z=10^6\text{V/cm}$.^[4]

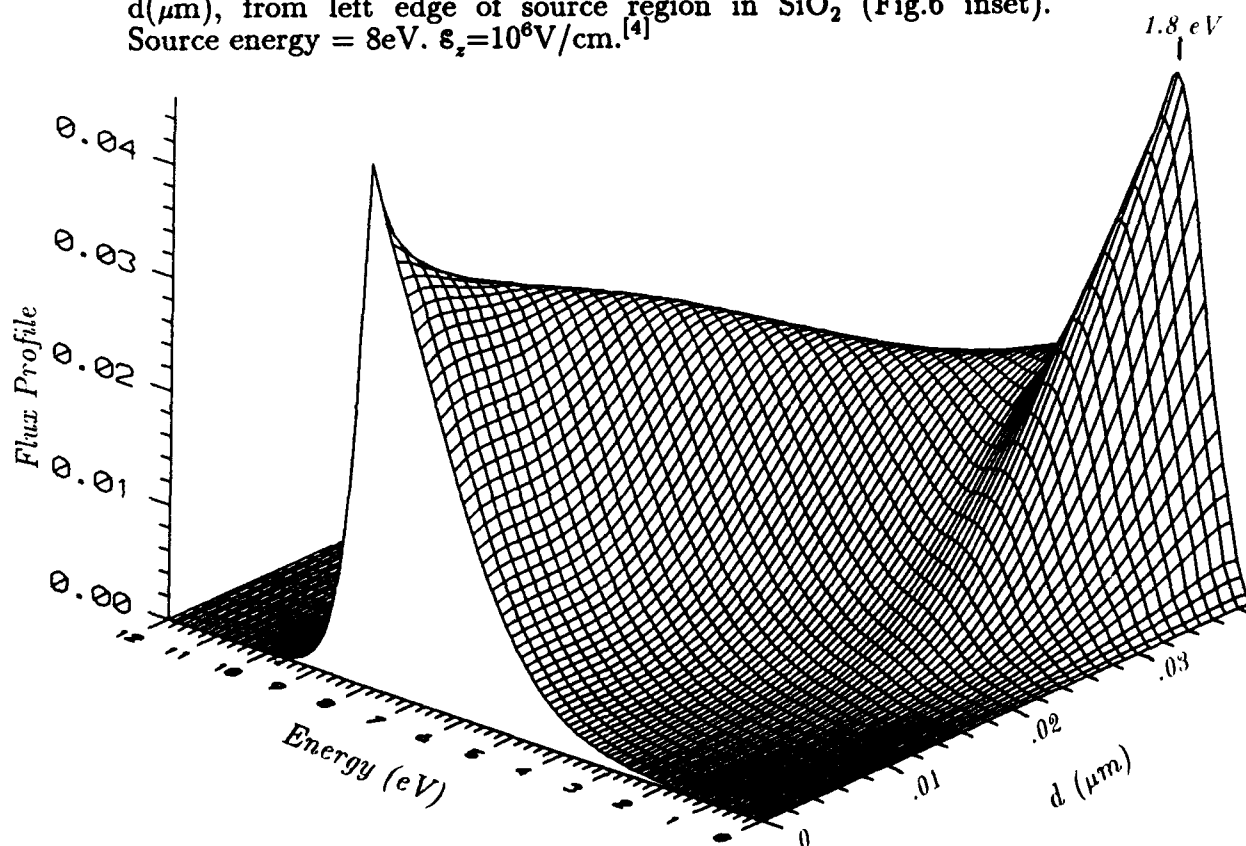


Fig. 8b. Electron energy flux spectrum profiles vs. distance, $d(\mu\text{m})$, from right edge of source region in SiO_2 (Fig.6 inset). Source energy = 8eV. $\mathcal{E}_z=10^6\text{V/cm}$.^[4]

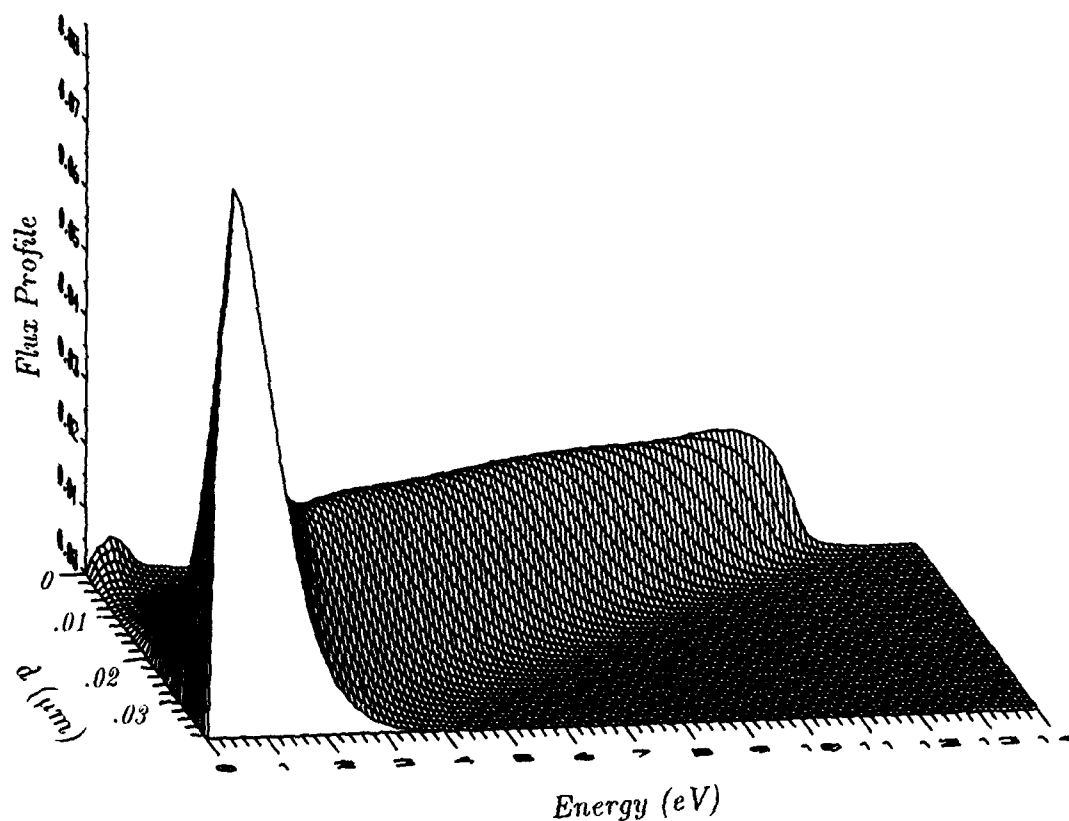


Fig. 9a. Electron energy flux spectrum profiles vs. distance, $d(\mu\text{m})$, from left edge of source region in SiO_2 (Fig.6 inset). Source energy = 12eV. $\epsilon_s = 2 \times 10^6 \text{V/cm}$.^[4]

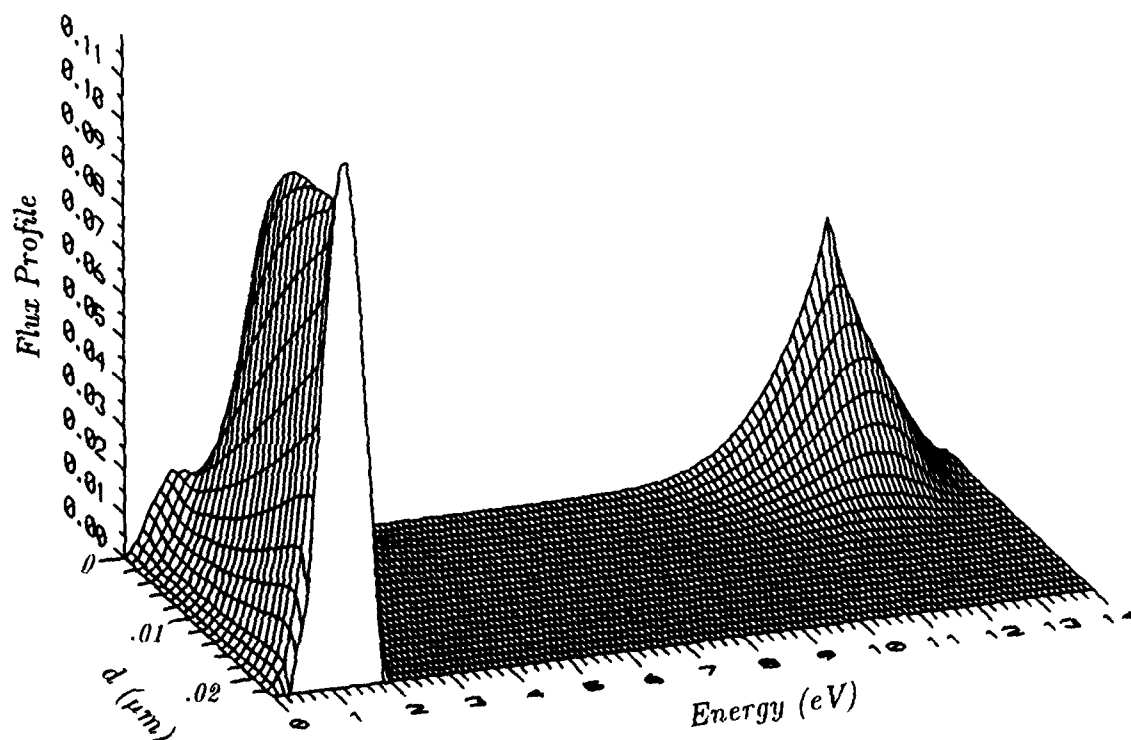


Fig. 9b. Electron energy flux spectrum profiles vs. distance, $d(\mu\text{m})$, from right edge of source region in SiO_2 (Fig.6 inset). Source energy = 12eV. $\epsilon_s = 2 \times 10^6 \text{V/cm}$.^[4]

2.4 The "Continuous Approximation" Restriction

In the calculations described in Sections 2.2 – 2.3, we found that imposition of the "continuous approximation"^[3] condition restricts the applicability of the S_N method to electron-phonon scattering problems. As previously stated, with this condition in force, a field-induced change in energy over one spatial discretization interval must not exceed one energy group width. That is,

$$e\mathcal{E}\Delta x \leq \Delta E_g . \quad (19)$$

For field strength values $\sim 5 - 10$ MV/cm and for $\Delta E_g \sim 0.1$ eV, the range of Δx values is $\sim 1 - 2\text{\AA}$. Typical SiO_2 slab thicknesses for these calculations were in the 500 - 1000 \AA range. A low energy transport calculation for 0 - 20 eV electrons can require $\sim 500 - 1000$ x -mesh cells and 100-200 energy groups. These requirements, combined with the probable necessity of running $\sim 20 - 40$ outer (energy group) iterations lead to a highly computationally intensive calculation. Based on these and other investigations described elsewhere in this document, we have concluded that the Monte Carlo method serves as well or better for calculations involving electron-phonon interactions.

III. Analytical Benchmark Verification of SNCODE Algorithm

1. Introduction

The S_N method is an approximate numerical method for the solution of the transport equation. Due to the fact that we generally obtained good S_N agreement with standard Monte Carlo calculations of energy deposition in solids, there was adequate reason to believe that the algorithms employed in SNCODE were providing "correct" answers. At the least, this agreement provided indication that the integrals of the scalar flux over energy checked out. This agreement did not, however, reveal much information pertaining to the accuracy of the flux calculations. A collaborative effort with B. D. Ganapol and J. C. Garth^[9] provided an excellent opportunity to monitor the accuracy of the spatial differencing algorithms of SNCODE. Ganapol developed a multigroup benchmark calculation that yielded exact determination of the group scalar fluxes for electrons. The availability of this benchmark method made it possible, for the first time, to make absolute determinations of the accuracy of the multigroup- S_N method as applied to electron transport. We give here a brief summary of the methodology and report some of the results obtained.

2. Multigroup Benchmark Calculations

The multigroup Boltzmann equation^[10,11] (Eq. 20) provides the theoretical basis for the approximate calculation of electron transport, scattering and energy loss in a planar infinite medium (in practical terms, a medium larger than one electron range).

$$\left(\mu \frac{\partial}{\partial x} + \frac{1}{\lambda_g}\right) \psi_g(x, \mu) = \sum_{g'=1}^g \sum_{\ell=0}^L \frac{2\ell+1}{2} \Sigma_{\ell g', g} P_{\ell}(\mu) \int_{-1}^1 d\mu' P_{\ell}(\mu') \psi_{g'}(x, \mu') + Q(\mu) \delta(x) \delta_{g,1}. \quad (20)$$

In the above, the notation and symbols have their usual standard definitions: $\psi_g(x, \mu)$ is the group g flux; λ_g is the group mean free path; and $\Sigma_{\ell g', g}$ are the group transfer cross sections, which are derived assuming applicability of continuous slowing down theory^[11].

As reported in Ref. 9, Ganapol derived an exact expression for the Legendre moments, $\phi_{g, \ell}$, of the Fourier transform of the group flux $\psi_g(x, \mu)$. He then performs a numerical inversion of the Fourier transform of the scalar group flux, $\phi_{g, 0}$, to obtain an exact determination of the scalar flux. The transform of the scalar flux is evaluated by solving a matrix equation involving sums over Legendre moments. The scalar flux can be evaluated to arbitrary accuracy, depending on the choice of the Legendre series order.

For our benchmark tests of SNCODE, we assumed an isotropic source, located at the center of the infinite medium, of electrons in the highest energy group ($g=1$), i.e.

$$Q(\mu) = \frac{1}{2}. \quad (21)$$

2.1 Results

The quantity taken as the basis for comparison of the S_N and benchmark calculations was the scalar flux. The approach taken in the comparisons between multigroup S_N and benchmark calculations began with a series of one-group calculations

for the plane isotropic source embedded in an essentially infinite aluminum medium in which the scattering cross section was taken to be linearly anisotropic. For this one-group case we investigated the behavior of the ratio of successive errors as the spatial mesh size was decreased in order to reproduce the known theory. The S_N and benchmark calculations were then made for the multigroup cases. These calculations, carried out using 40 uniformly spaced electron energy groups, were made for a 200 keV electron source in aluminum. Four scattering cases, corresponding to progressively higher scattering anisotropy order, were investigated. In the first, an artificial isotropic scattering cross section was devised, and in the remaining four, S_N and benchmark calculations were compared for extended transport corrected cross sections of order 2 through 4.

Because the benchmark calculations can only accommodate an infinite medium, and the S_N algorithm requires a finite medium, we chose the dimensions of the test mesh portions of the scattering media to be deeply imbedded within two very thick coarsely meshed slabs each of thickness 10 mean free paths. For the multigroup calculations, we chose the slab dimensions to correspond to ± 1 r.u. (= range unit), which for our 200 keV electron source in aluminum translates into a thickness of ± 0.058 g/cm². These geometries closely approximate infinite media for all practical purposes.

2.1.1 Plane Isotropic Source; One-Group; Linearly Anisotropic Scattering

A set of 5 S_{12} calculations were made with the linear discontinuous differencing algorithm for a plane isotropic source located at the center ($x=0$) of a thick scattering medium extending 20 mean free paths in both positive and negative x -directions. The scattering parameters were (in units of mean free path), $\Sigma_t = 1.0$, $\Sigma_{s0} = 0.8$, $\Sigma_{s1} = \Sigma_{s0}/3$. The spatial mesh discretization step sizes for the 5 calculations were taken to be $\Delta x_n = 2^{2-n}$; $n=1,2,3,4,5$. In each calculation, Δx was held constant over the spatial mesh test region ($-10 \leq x \leq +10$). Figure 10 is a plot of the successive error ratios $r_n(x)$ [$\equiv \epsilon_n(x)/\epsilon_{n+1}(x)$]. From the curves shown, a region of uniformity ($3 \lesssim |x| \lesssim 6$) could be identified for successive discretization error ratios. In this region it was found that the error always decreased for $n=1,2,3$. For the $n=1$ and $n=2$ cases, the ratio is nearly constant and has the value ~ 8 , which indicates second order accurate behavior for the linear discontinuous algorithm (when the error decreases as the exponent n , the approximation is said to be $(n-1)$ order accurate). Also in this region, when $n=3$, it is seen that the error ratio settles down to ~ 8 for one-half of the interval; however, the ratio r_4 does not show a consistent decrease in error as Δx is decreased from 0.25 to 0.125. This is attributable to the fact that it is not possible to further improve the result by halving Δx with a fixed inner iteration convergence precision. The fractional errors observed in these cases were generally comparable to the convergence precision (10^{-5}). Large variations in r_n were observed both near the source plane and the region boundary. The poor results near the source plane arise from the singular nature of the source geometry, while near the region boundary, changes in mesh size propagate errors into the test zone. The uniform region is situated well away from both.

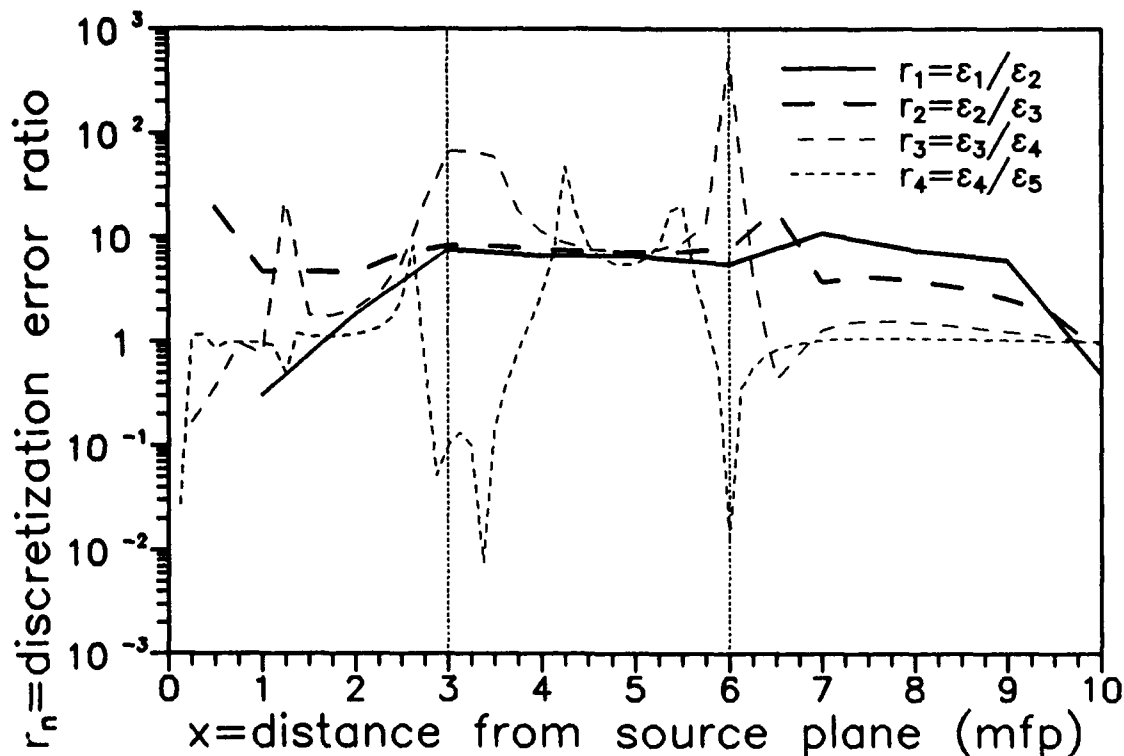


Fig. 10. Ratios of successive errors for 5 one-group linear discontinuous S_{12} calculations. Spatial discretization step size is varied according to $\Delta x_n = 2^{2-n}$; $n=1-5$. Stable region, $3 \leq |x| \leq 6$ (mean free path units), is indicated.^[9]

2.1.2 Plane Isotropic Source; Multigroup; Isotropic Scattering

Four sets of SNCODE calculations were made for the 200 keV isotropic electron source imbedded in infinite aluminum. The scattering cross section employed for these calculations is physically unrealistic in that 200 keV electrons in aluminum do not scatter isotropically. However in this first attempt to test the multigroup benchmark, we chose for convenience a cross section which contains only the zero-th order Legendre coefficient of the P-12 extended transport corrected Mott cross section. These calculations covered the following four cases: linear discontinuous and diamond differencing, each used with S_6 and S_{12} Gauss-Legendre quadrature sets. In each of these four cases, 5 separate S_N calculations were made, corresponding to a graduated scale of spatial mesh resolutions [$\Delta x = .02, .01, .004, .002, .001$ r.u.] spanning a distance of 0.2 r.u. from the source plane at $x=0$. The reasons for the restriction to 0.2 r.u. are twofold: 1) to eliminate vacuum boundary effects in the S_N calculations; 2) to operate within the high accuracy range of the analytical benchmark solution.

As will be apparent in the graphs of Figs. 11 and 12 it was found that the differences between S_6 and S_{12} calculations were for practical purposes negligible. Figure 11 is a plot of the scalar flux as calculated by the benchmark method (solid lines) and SNCODE- S_6 (circles) with the diamond difference scheme for spatial resolution $\Delta x = .004$ r.u. The 10 curves are the energy spectra at $x = .02(.02).2$ r.u. As can be seen, the agreement is excellent. Figure 12 is a plot for the identical conditions except that the S_N calculation was made with SNCODE- S_{12} . While little or no sensitivity to discrete ordinate order n was observed in these two calculations, we did find that the accuracy of the SNCODE calculations was highly sensitive to the spatial discretization. In Figure 13 we show the same case as given in Figure 12 (diamond difference, S_{12} , isotropic scatter), however the spatial mesh resolution was coarsened to $\Delta x = .01$ r.u. Here we observe significant departures from the agreement obtained with $\Delta x = .004$ r.u.

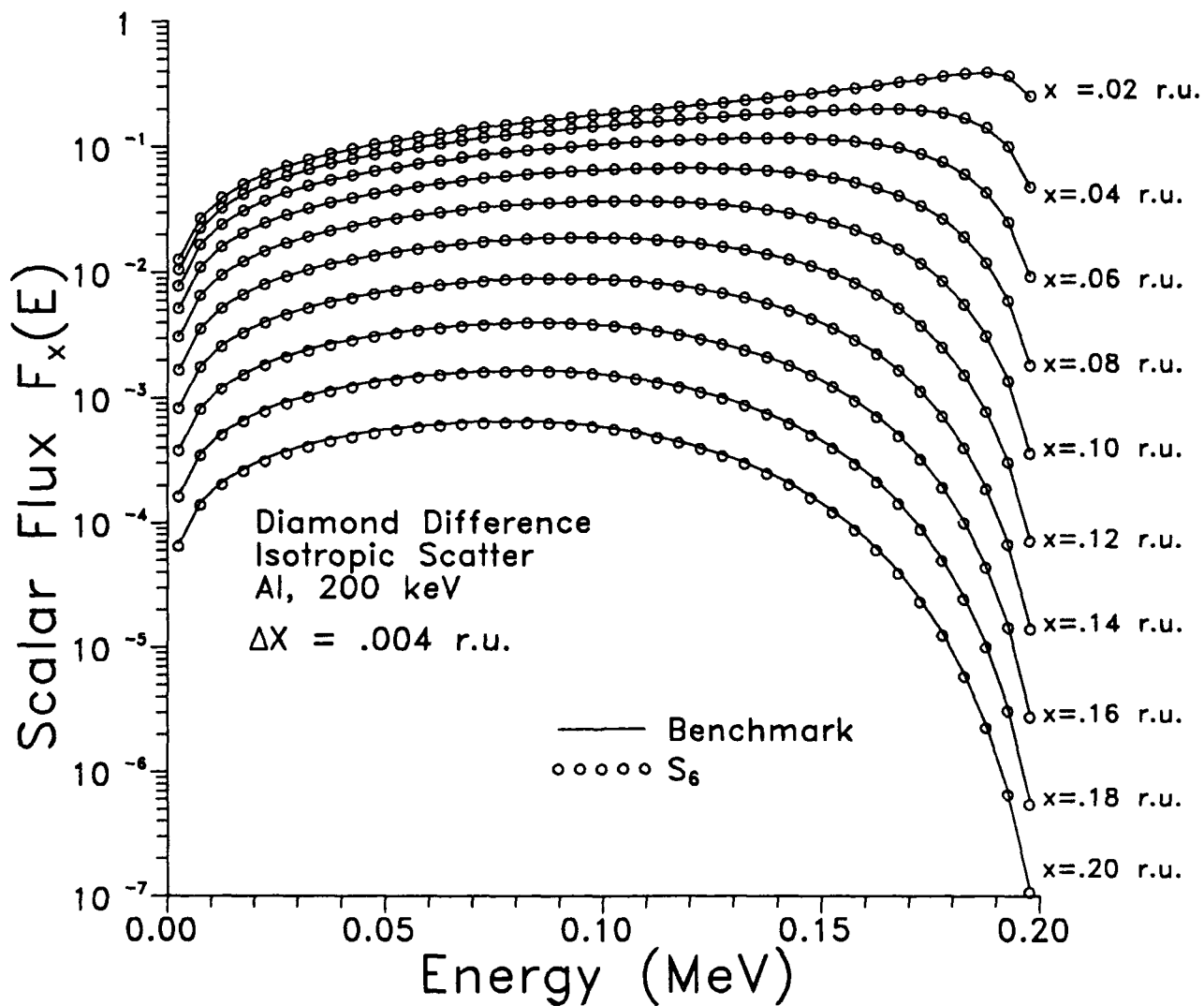


Fig. 11. Comparison of the scalar flux, $F_x(E)$ vs. E , for 40 energy groups at 10 x positions as indicated. Solid lines represent the benchmark calculation results; circles represent the results of a diamond difference SNCODE- S_6 calculation. x -discretization interval $\Delta x = 0.004$ range units. ^[9]

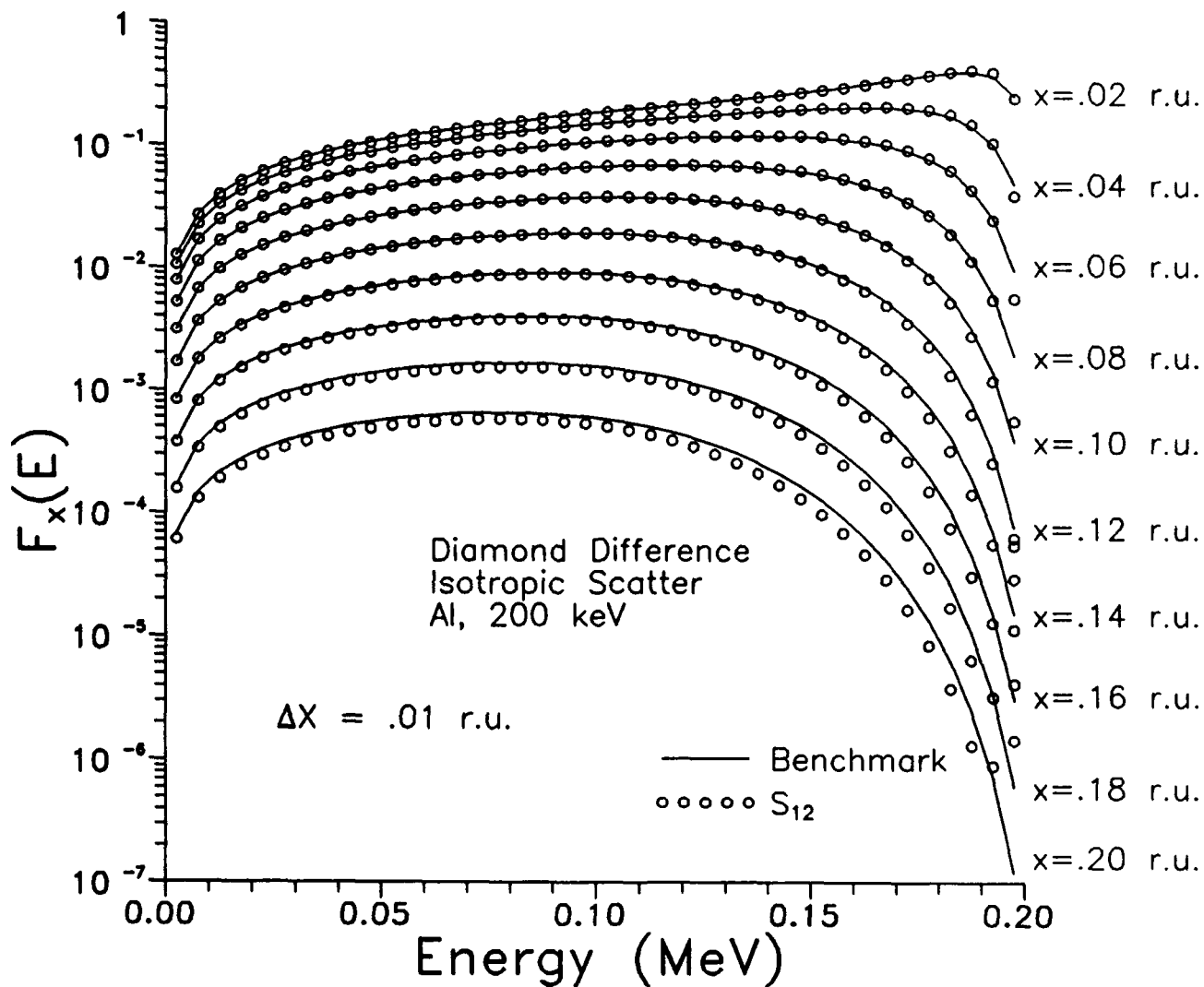


Fig. 12. Comparison of the scalar flux, $F_x(E)$ vs. E , for 40 energy groups at 10 x positions as indicated. Solid lines represent the benchmark calculation results; circles represent the results of a diamond difference SNCODE_{S₁₂} calculation. x -discretization interval $\Delta x = 0.01$ range units.^[9]

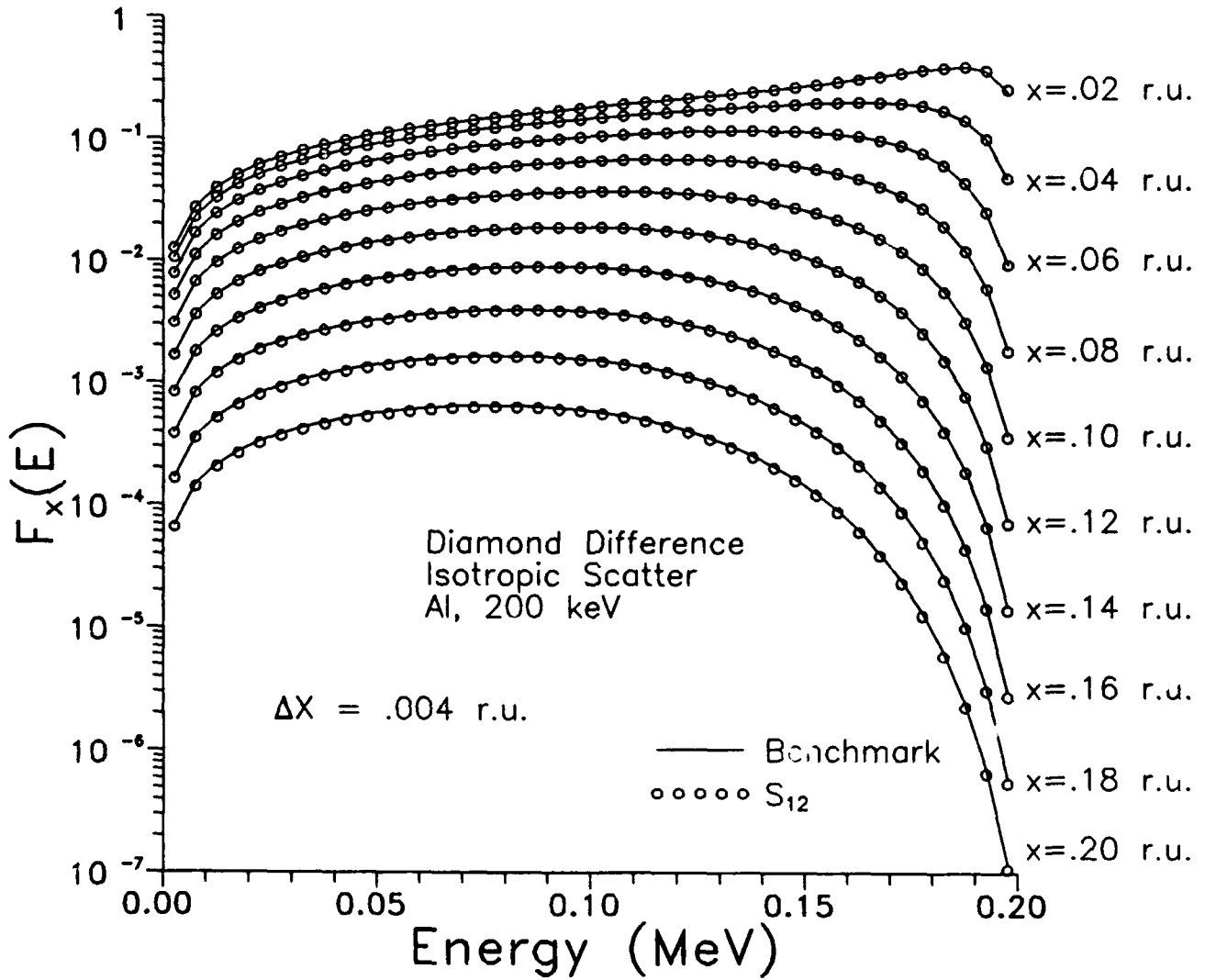


Fig. 13. Comparison of the scalar flux, $F_x(E)$ vs. E , for 40 energy groups at 10 x positions as indicated. Solid lines represent the benchmark calculation results; circles represent the results of a diamond difference SNCODE- S_{12} calculation. x -discretization interval $\Delta x = 0.004$ range units. [9]

2.1.3 Relation Between Spatial Resolution and Discretization Error

To further examine the sensitivity of S_N calculations to spatial discretization, we made a study of the dependence of discretization error on resolution. Having a set of true benchmark calculations enabled this. Figure 14 is a plot of the exponent, b , of the relative error dependence [$\epsilon \propto (\Delta x)^{-b}$] of the spatial resolution vs. group midpoint energy, for 6 positions along x , as the resolution is increased from $\Delta x = .02$ to $\Delta x = .01$ r.u. for the linear discontinuous algorithm. The relative error (ϵ) was evaluated as the deviation of the S_N result from the benchmark result. The inner iteration convergence precision for the upper graph was set to 10^{-3} , while for the lower graph, we chose 10^{-5} . As anticipated, the exponent is -3 as dictated by theory. It should be noted that this holds true for a wider energy range as the accuracy of the S_N calculation was increased. However, at some point sufficiently low on the energy scale, no further improvement was achieved. As might be expected, the more accurate S_N calculation, to the extent that this crossover behavior exists at all, exhibited this behavior at a lower energy value. We believe that this is explained by an accumulation of the downscatter source error, which is not predominant in the high energy groups. It can also be noted that tightening of the convergence precision mitigated most of the erratic behavior of the exponent at the two positions ($x = .02, .06$ r.u.) closest to the source plane.

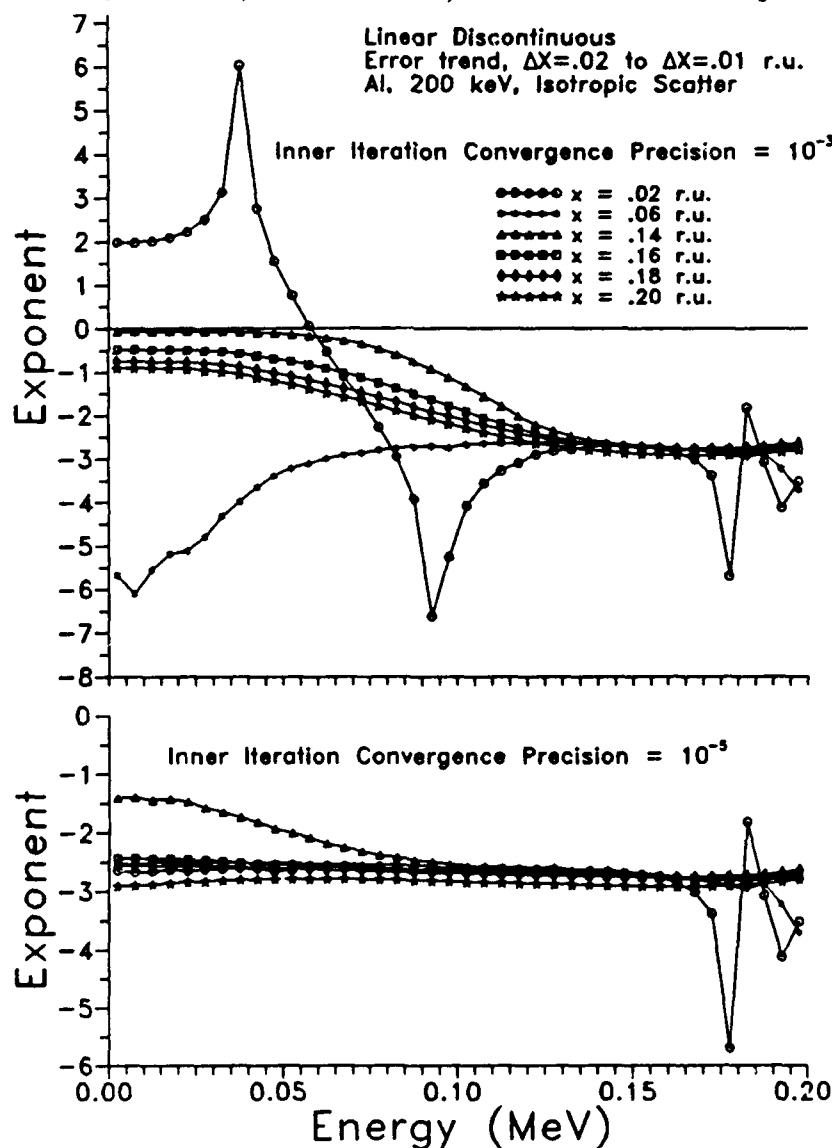


Fig. 14. Plots of the exponent [b] of the relative error [ϵ], where $\epsilon \propto \Delta x^{-b}$, as Δx is decreased from .02 to .01 r.u. The behavior of b is shown as a function of energy at the six x positions indicated for two linear discontinuous S_6 calculations with inner iteration convergence precisions given by 10^{-3} (upper graph) and 10^{-5} (lower graph)^[9].

2.1.4 Plane Isotropic Source; Anisotropic Scattering

The 200 keV electron source (at $x=0$) and aluminum scatterer configuration ($|x| \leq 1.0$ r.u.) chosen for the anisotropic scattering benchmark tests were the same as those used in the previous isotropic scattering case. It had already been demonstrated^[11,12] that a realistic description of the transport, or at least the resultant energy deposition, of 200 keV electrons in aluminum could be achieved using a P-12 extended transport corrected screened-Rutherford scattering cross section in conjunction with the S_N method. At the risk of sacrificing physical realism, we made successive application of the extended transport correction from P-1 to P-4 to solve the "same" problem if only approximately. This provided us with a means for systematically increasing the scattering anisotropy order of the benchmark calculations. Figures 15-17 show plots of the scalar flux at 10 equispaced x values $[0.04(0.04)0.4]$ for the P-2, P-3 and P-4 extended transport corrected cross sections (the L -th Legendre coefficient of the P-L extended transport cross section is zero, hence these represent scattering anisotropy orders 1,2,3). In all cases the linear discontinuous differencing algorithm was employed in 40 group SNCODE- S_{12} calculations. The spatial discretization step was held constant at $\Delta x=0.002$ r.u. As before, the solid curves represent the benchmark solution. The agreement between the two methods ranges between the third and fifth significant figure for all points except at the source plane.

These investigations served not only as a demonstration of the first multigroup benchmark transport solution, but also as a validation of the operation of SNCODE. It should be pointed out that the benchmark algorithm is analytically exact in spatial dependence only. Both S_N and benchmark calculations treat energy dependence identically. The two calculation methods, multigroup- S_N and benchmark, complemented one another. The excellent agreement between multigroup- S_N and the benchmark results: 1) provided verification of the predicted error behavior for both the linear discontinuous and diamond difference schemes; and 2) allowed us to proceed more confidently to more realistic S_N electron transport calculations with SNCODE.

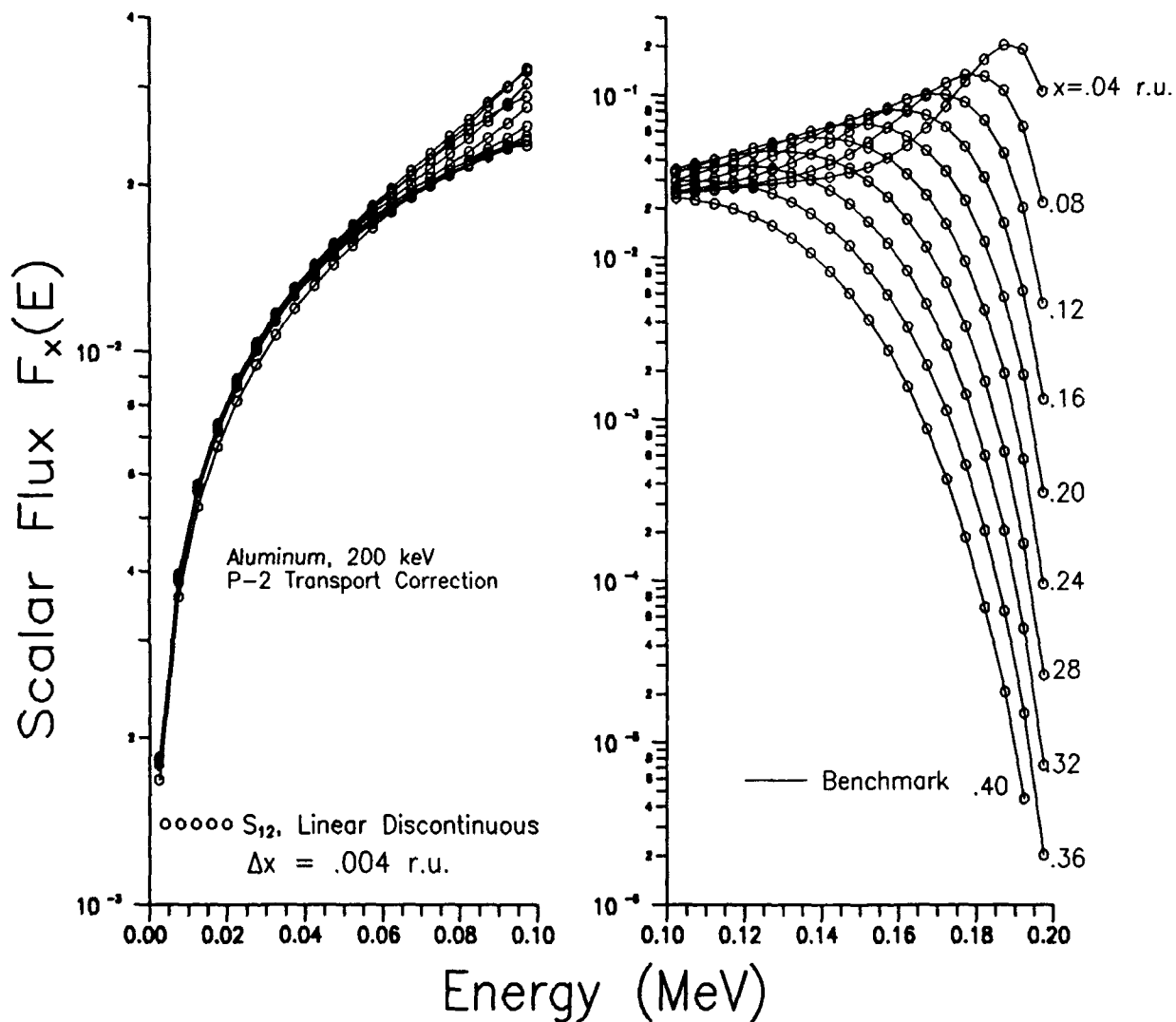


Fig. 15. Comparison of the scalar flux, $F_x(E)$ vs. E , for 40 energy groups at 10 x positions as indicated. Solid lines represent the benchmark calculation results; circles represent the results of a linear discontinuous SNCODE- S_{12} calculation. Anisotropic scattering of 200 keV electrons in Al with P-2 extended transport corrected cross sections. ^[9]

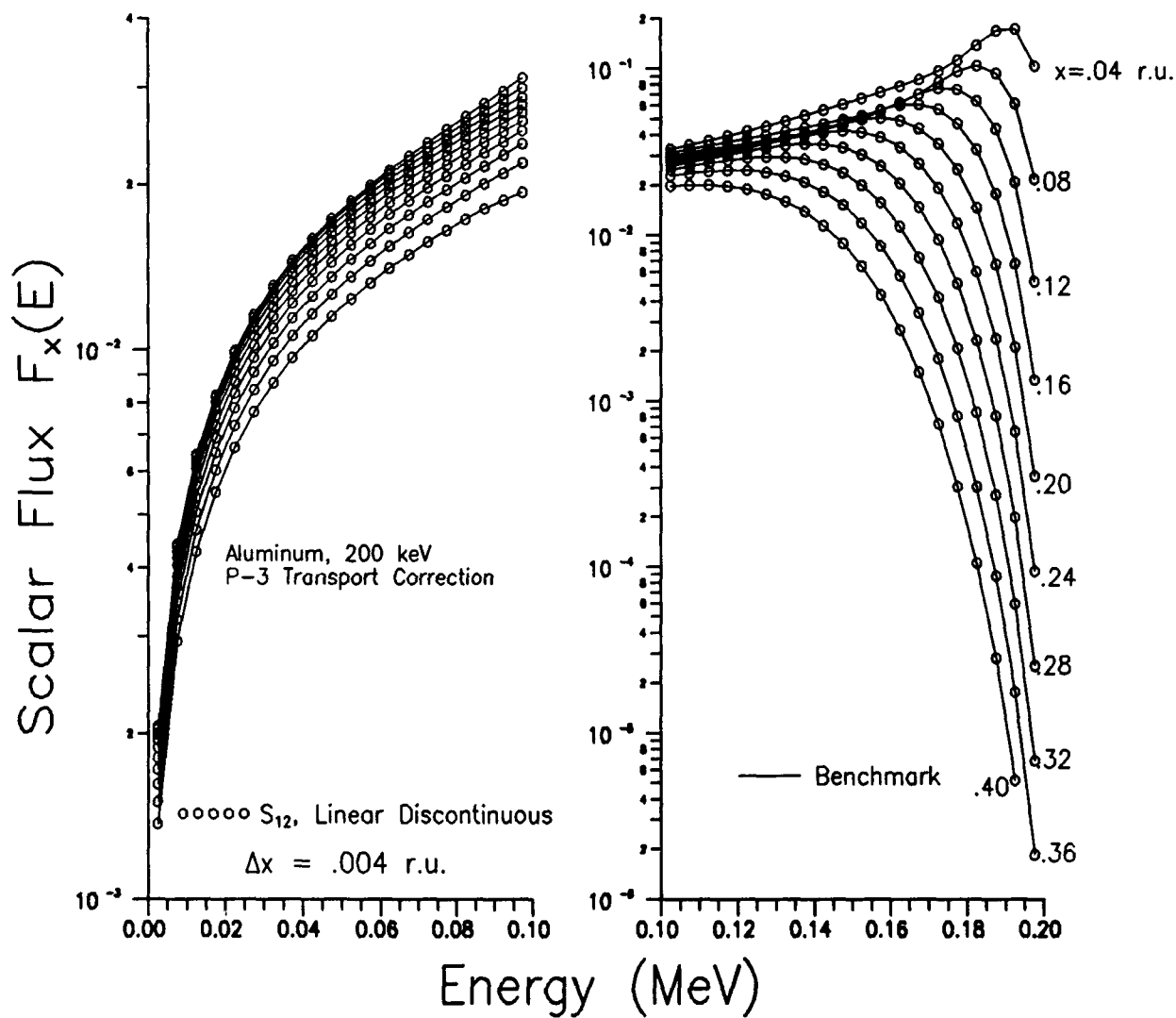


Fig. 16. Comparison of the scalar flux, $F_x(E)$ vs. E , for 40 energy groups at 10 x positions as indicated. Solid lines represent the benchmark calculation results; circles represent the results of a linear discontinuous SNCODE- S_{12} calculation. Anisotropic scattering of 200 keV electrons in Al with P-3 extended transport corrected cross sections. ^[9]

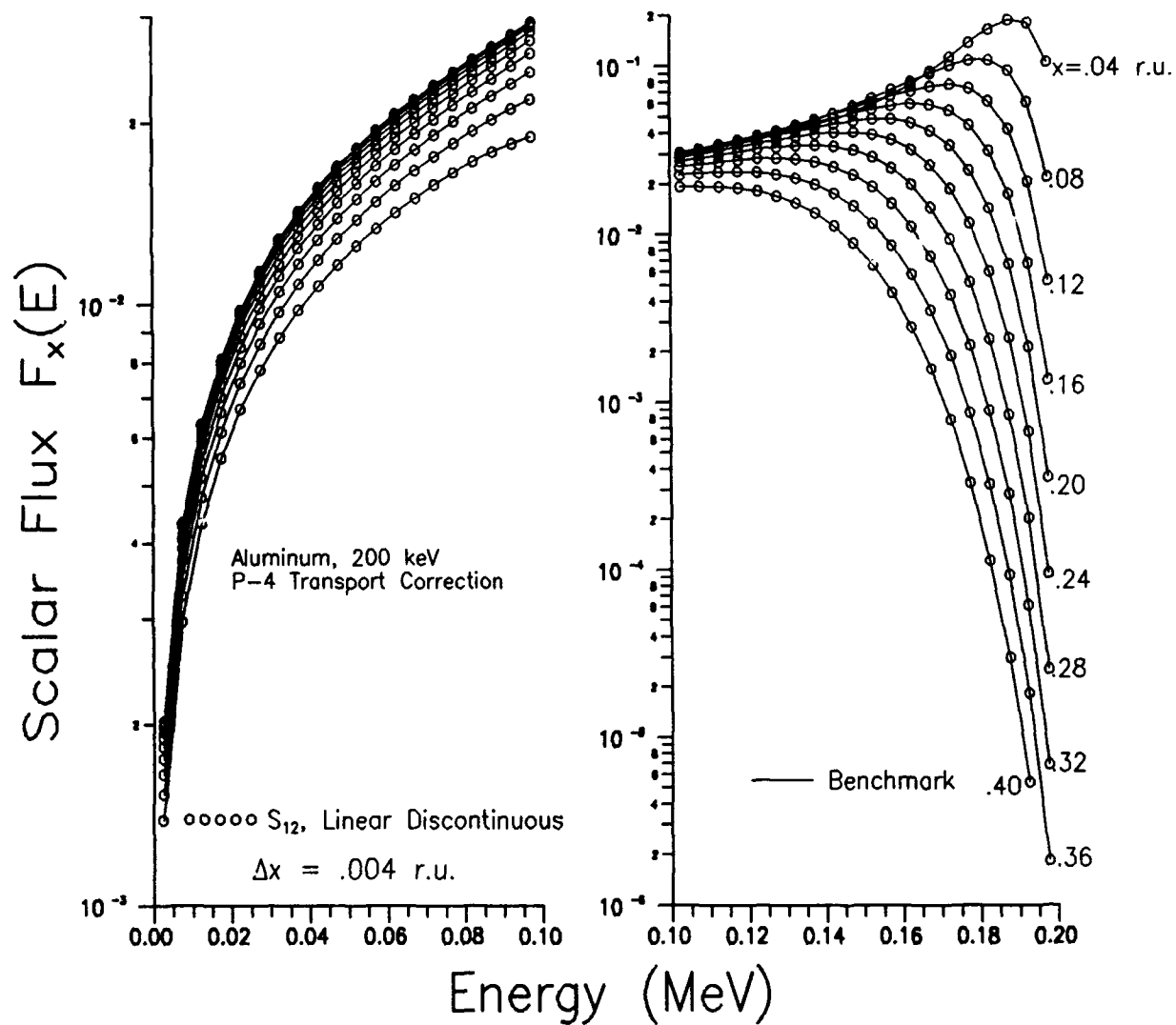


Fig. 17. Comparison of the scalar flux, $F_x(E)$ vs. E , for 40 energy groups at 10 x positions as indicated. Solid lines represent the benchmark calculation results; circles represent the results of a linear discontinuous SNCODE- S_{12} calculation. Anisotropic scattering of 200 keV electrons in Al with P-4 extended transport corrected cross sections. ^[9]

3. Analytical Benchmark Testing of One-Group SNCODE Calculations with a Material Discontinuity

Another series of analytical benchmark tests were conducted for the verification of SNCODE. The objective of this research, a collaborative effort with B. D. Ganapol and J. C. Garth^[13], was the development of an analytical benchmark calculation for one-group neutron transport in an infinite medium with a material discontinuity. Participation in this research effort provided an opportunity for using SNCODE to confirm the validity of the analytical benchmark solution and also resulted in an evaluation of the accuracy of SNCODE for one-group transport in dissimilar media.

The analytical solution for two interfacing half spaces of dissimilar material was obtained using a numerical Laplace transform inversion which has proven to be successful for single half-space problems^[14]. Isotropic scattering was assumed with a general spatially distributed isotropically emitting source in the right half-space. The solution developed in Ref. 13 was used to benchmark an SNCODE which was written primarily for application to electron transport where material boundaries have a profound influence.

3.1 Uniformly Distributed Source

In Figure 18 a comparison between the analytical benchmark and SNCODE is shown for S_2 , S_4 , S_6 , and S_{12} calculations. Isotropic scattering was assumed, and the albedos for the left- and right-hand half-spaces were $c_2 = 0.8$, $c_1 = 0.95$, respectively. A uniform isotropic source is distributed throughout the right half-space. Note that, as required, the flux for large x approaches $1/(1 - c_1) = 20$. For 6 and 12 ordinates, the results are virtually indistinguishable from the analytical solution. As will be shown, this close agreement did not generally hold for sources located at the interface.

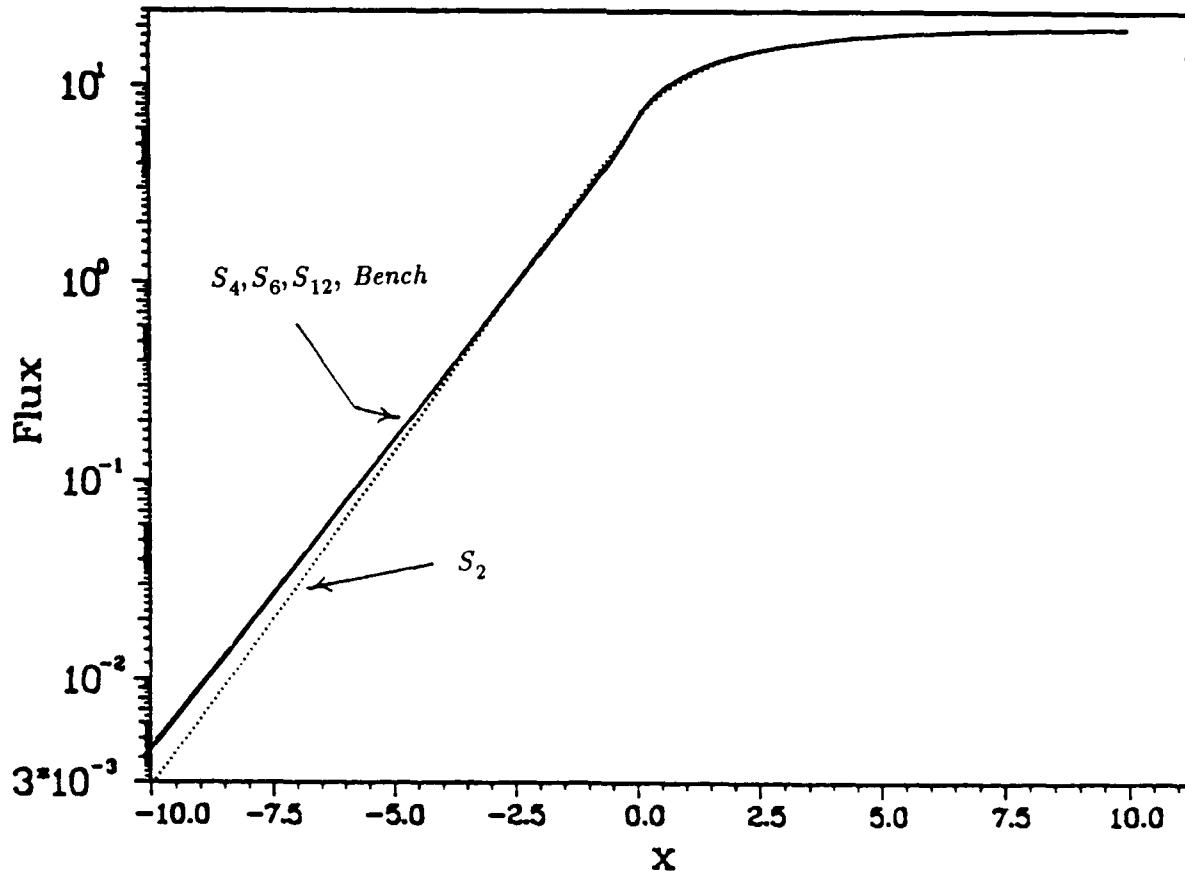


Fig. 18. Comparison of SNCODE discrete ordinates and benchmark results (S_2 , S_4 , S_6 and S_{12})^[13].

3.2 Plane Isotropic Source

Several test runs were made for a plane isotropic source located at the interface between two dissimilar media. Every possible combination of c_1 and c_2 for $c = .8, .9, .95$ and $.99$ was tested. The SNCODE calculations were made for S_2 , S_{12} and S_{20} , thus providing a wide range of angular quadrature precision. As the order of the S_N calculation was increased, the approximate result more closely approached the analytical benchmark, as anticipated. However, even the S_{20} calculation did not closely match the benchmark curve near the material interface. Figures 19 and 20 show the plane source results for $c_2 = 0.8$, $c_1 = 0.95$, and $c_2 = 0.95$, $c_1 = 0.8$, respectively. We found that, for these calculations, increasing the angular quadrature precision alone provided limited improvement in the accuracy of the results. Better agreement near the interface was obtained when the spatial discretization resolution was increased along with the quadrature order.

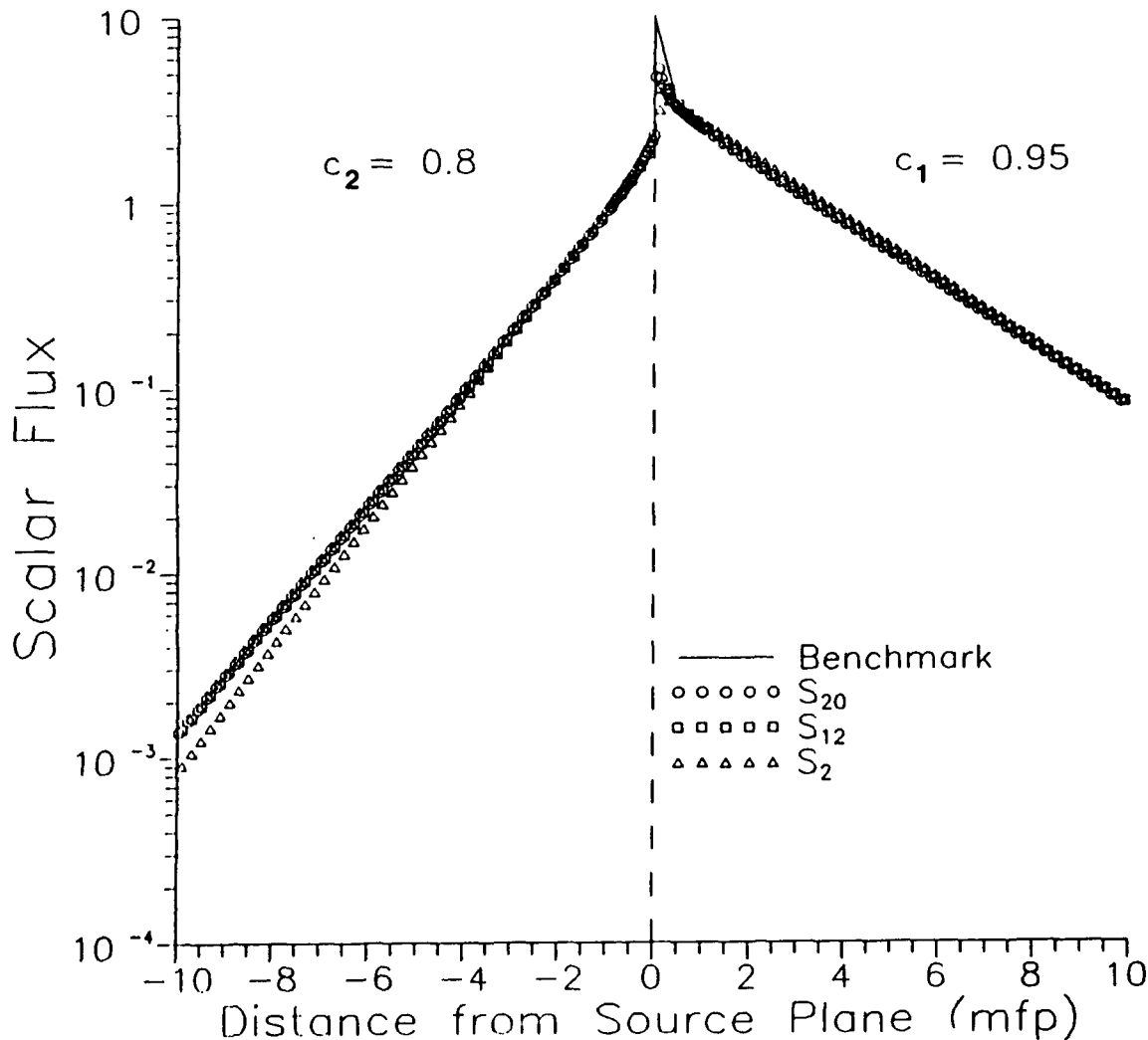


Fig. 19. Comparison of SNCODE- S_2 , S_{12} , S_{20} and benchmark scalar flux results as a function of distance from the material interface-source plane ($c_2 = 0.8, c_1 = 0.95$)^[13].

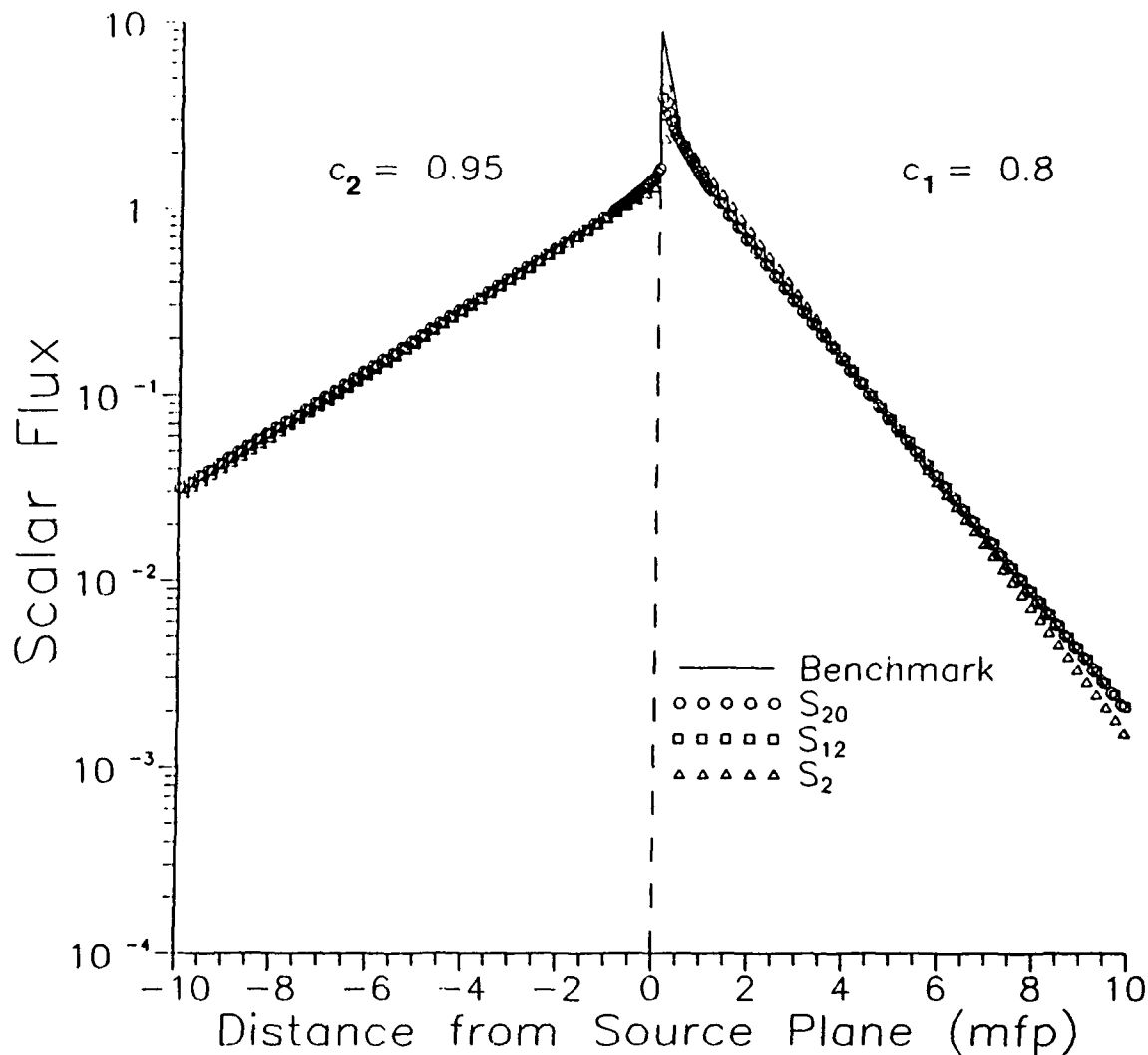


Fig. 20. Comparison of SNCODE- S_2, S_{12}, S_{20} and benchmark scalar flux results as a function of distance from the material interface-source plane ($c_2 = 0.95, c_1 = 0.8$)^[13].

4. Analytical Benchmark Testing of One-Group SNCODE Calculations in Half-Space Geometry

In addition to the infinite medium electron and neutral particle transport investigations described above, a further collaboration with B. D. Ganapol and J. C. Garth^[13] has recently been initiated and continues to the present. This is a series of analytical benchmark calculations were made and then used to test the performance of the S_N algorithms of SNCODE. The analytical benchmark calculation was formulated by Ganapol for one-group neutral particle transport in half-space geometry, and is also based on the Laplace transform inversion method^[14]. A variety of source configurations have been tested. Of these, the major effort has been directed thus far toward boundary source problems. An example of our results is given in Figure 21. Here we have shown a benchmark solution (solid curve) for the scalar flux in a semi-infinite, isotropically scattering medium with albedo $c = 0.5$ where the source is specified by the flux boundary condition

$$f(\mu) = Ae^{-(1-\mu^2)^{-1}}, \quad (22)$$

where A is the normalization constant. Four S_N calculations were made, corresponding to $n = 6, 12, 20, 30$. It is apparent from the graphs of Fig. 21 that the S_N and

benchmark calculations converge, as in the previously presented results. This work is presently in progress, and benchmark comparisons will be made not only for several source configurations, but also for other independent calculation methods such as iterative solutions of the integral form of the Boltzmann equation.

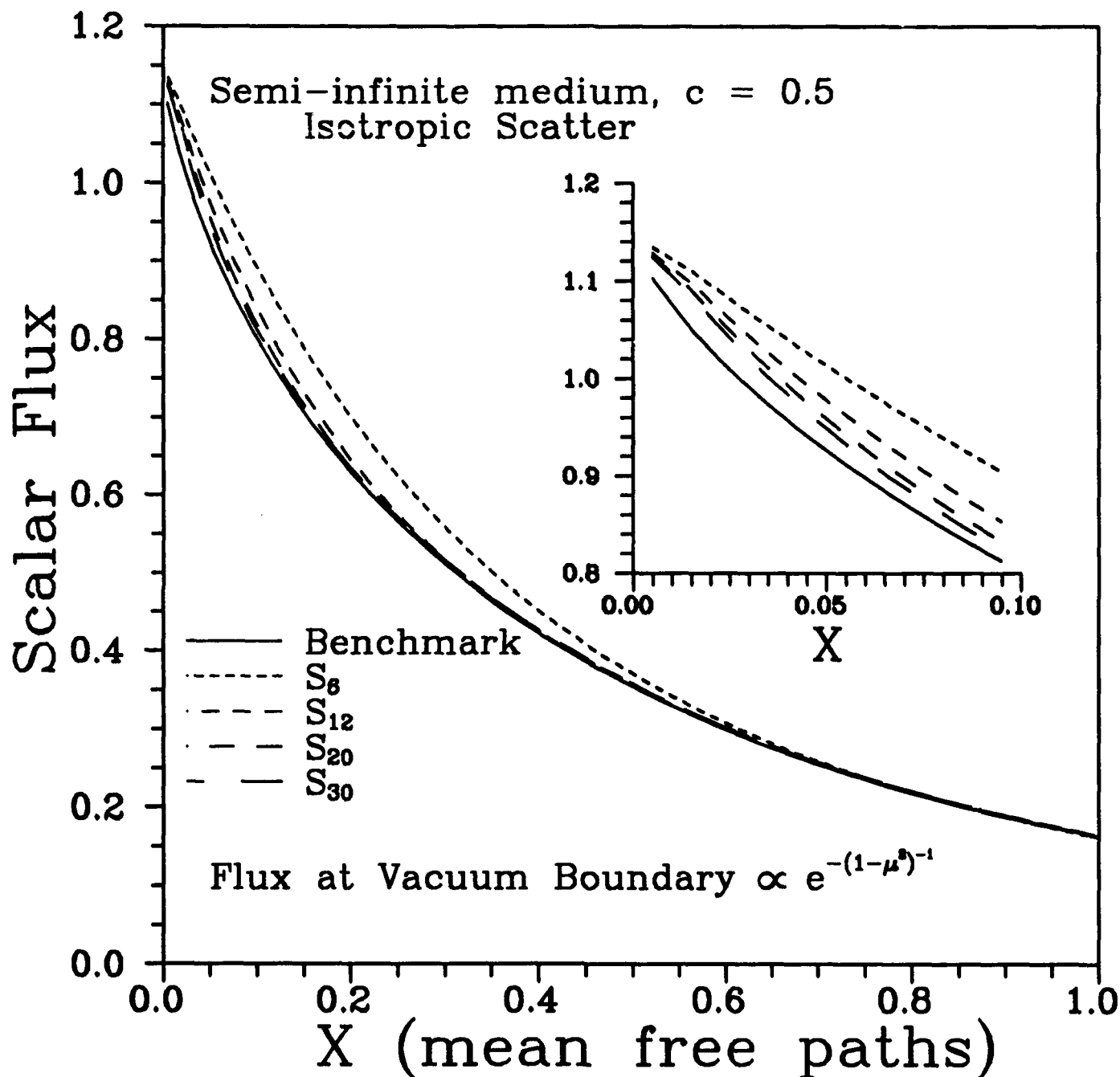


Fig. 21. Comparison of analytical benchmark and S_N determinations of scalar flux vs. x in an isotropically scattering medium ($c = 0.5$) for $e^{-1/(1-\mu^s)}$ flux entering free surface. Solid curve represents analytical solution; dashed curves represent SNCODE- $S_6, S_{12}, S_{20}, S_{30}$ solutions^[15].

IV. Monte Carlo Transport Calculations for Electrons in Strong Electric Fields in Silicon Dioxide^[16]

1. Introduction

Transport calculations^[16] for electrons in the presence of a strong electric field in the oxide layer of an idealized MOS device were made with the LOWEND^[5] Monte Carlo code. In the electron energy range $8.9 \text{ eV} < E < 20 \text{ eV}$, where two processes, electron-phonon scatter and electron-electron scatter overlap, it was reasonable to expect that a significant amount of impact ionization should occur, since calculated electron energy spectra in the presence of strong electric fields have high energy tails, resulting from energy promotion by the electric field and phonon absorption, extending well beyond the ionization threshold ($E_{gap} = 8.9 \text{ eV}$). One motivation for this investigation was an attempt to explain the apparent inability to experimentally observe substantial secondary electron production in SiO_2 and the high energy tail observed in the vacuum emission spectra^[17-19]. A complete report of the results of these Monte Carlo studies is given in Ref. 16, a collaborative effort with J. N. Bradford.

2. Discussion

In this work we demonstrated how: 1) a revised calculation of the ionization cross section; 2) a change in the value of the deformation potential in acoustic phonon scatter; and 3) variation of the electric field profile as a result of negative charge trapping in the oxide reduce the high energy tail of the electron spectrum. These three items combine to produce a substantial reduction in secondary electron production. Further, in order to simulate experimental conditions as closely as possible, we added a transport calculation through a 200 Å aluminum coating at the anode side of the oxide layer. For this we made calculations of inelastic electron-electron scattering cross sections based on the Tung-Ritchie^[20] dielectric response function and then wrote a separate Monte Carlo code incorporating these cross sections.

A revision of the impact ionization cross section curve^[7] for SiO_2 was calculated based on the Anderson-Crowell^[22] ionization threshold value E_{th} . Their corrected value for E_{th} is 11.9 eV, as contrasted with the generally accepted 8.9 eV value, and is determined through an assertion that the ionization threshold is dependent on the ratio of the electron effective mass values for the valence and conduction bands. As can be seen from the two curves shown in Figure 22, the inverse mean free path (or cross section) for impact ionization is significantly lowered as a result of the upward shift in E_{th} . This combined with the fact that ionization cannot occur for energies less than 11.9 eV rather than 8.9 eV, resulted in lowering the production of secondary electrons.

The effects of a change in the acoustic phonon scatter deformation potential and oxide charging on secondary electron production were studied with the original impact ionization cross sections ($E_{th} = E_{gap}$). This was done in order to isolate these factors from changes in the ionization cross section. Figure 23 shows the fraction of secondary electrons produced at 600 Å penetration depth in the oxide as calculated by LOWEND. The effects of increasing the deformation potential from 3.5 eV to 5.0 eV and oxide charging are investigated separately. The charged oxide condition was simulated by specifying an anode field of 8 MV/cm which decreases linearly to zero at the cathode end, resulting in an average field value of 4 MV/cm in the oxide layer. Contrasted with this are LOWEND runs in which the field value is held constant at 4 MV/cm across the oxide layer. This simulates an uncharged oxide with the same field strength as the charged oxide average field strength. The combined effect of increased deformation potential and oxide charging is considerably lower secondary electron production.

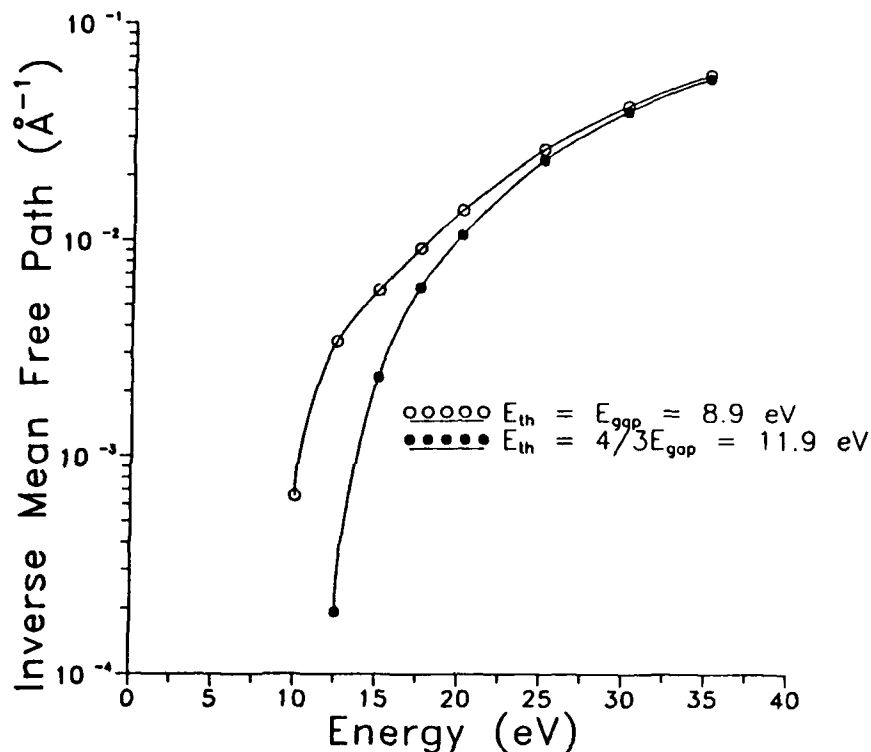


Fig. 22. Change in inverse mean free path for impact ionization according to the Anderson-Crowell formula. Results for threshold energy of $4/3E_{gap}$ as calculated by Ashley^[16,22].

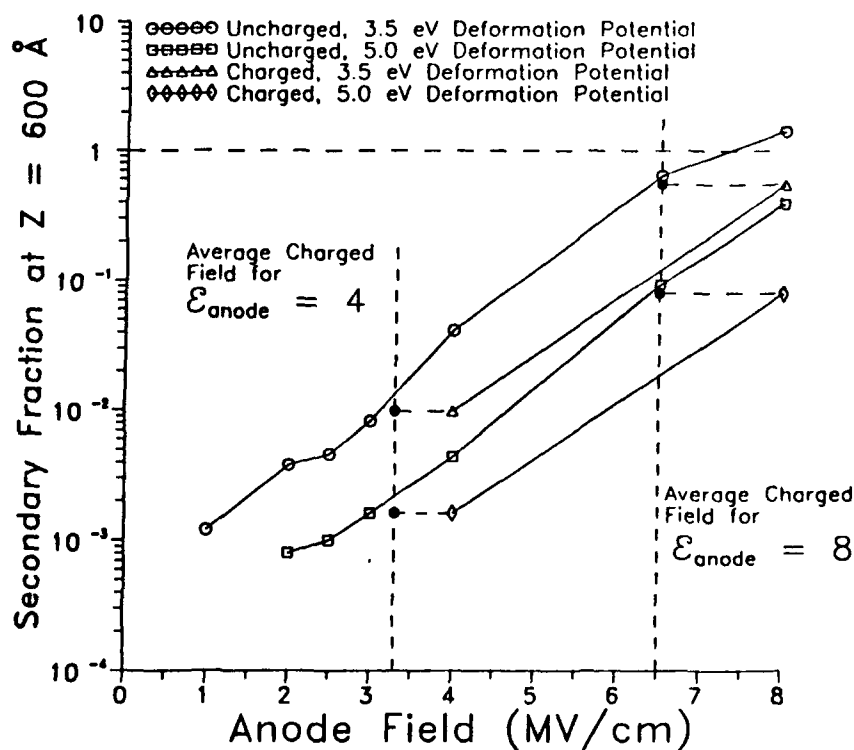


Fig. 23. Fraction of secondary electrons produced by 5000 primary electron case histories in traversing 600Å penetration depth. Charged oxide values are shown, by backward projection, to equal those from uncharged oxide with field equal to average of charged oxide field^[16].

The LOWEND Monte Carlo code was also used to calculate the vacuum emission kinetic energy spectra with the 5 eV deformation potential, with and without oxide charging. The spectra shown in Figure 24 were obtained with two electric field configurations: linearly varying field, 8 MV/cm at the anode with average value 6 MV/cm (solid histogram); and constant electric field throughout, 8 MV/cm (dashed histogram). The two cases shown illustrate that the value of the field at the anode, and *not* the average field value, determines the energy spectrum shape. The second spectrum graph, Figure 25, further demonstrates the important role of the anode field value. The two spectra shown here result from different anode field values, 8 MV/cm and 6 MV/cm. The average field for both spectra is 6 MV/cm. One case (solid histogram) corresponds to a constant 6 MV/cm field, and the other (dashed histogram) to a linearly varying field.

Finally, we performed a Monte Carlo simulation of the transport of electrons emitted from the oxide layer through a 200Å thick aluminum anode. The input spectrum from the SiO₂ was the spectrum shown for the 8MV/cm anode field (Fig. 24, solid histogram). The inelastic electron-electron cross sections were calculated using the electron gas model of Tung and Ritchie^[20] which is outlined in Section 2.1.

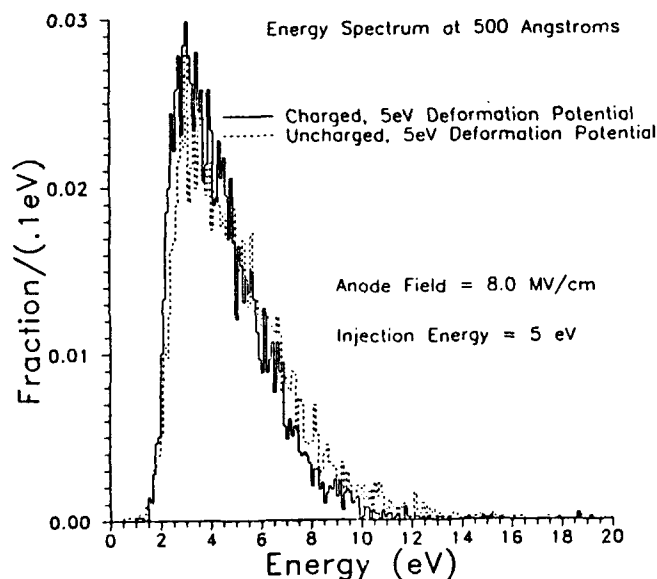


Fig. 24. Kinetic energy spectra from charged and uncharged oxides with same anode field^[16].

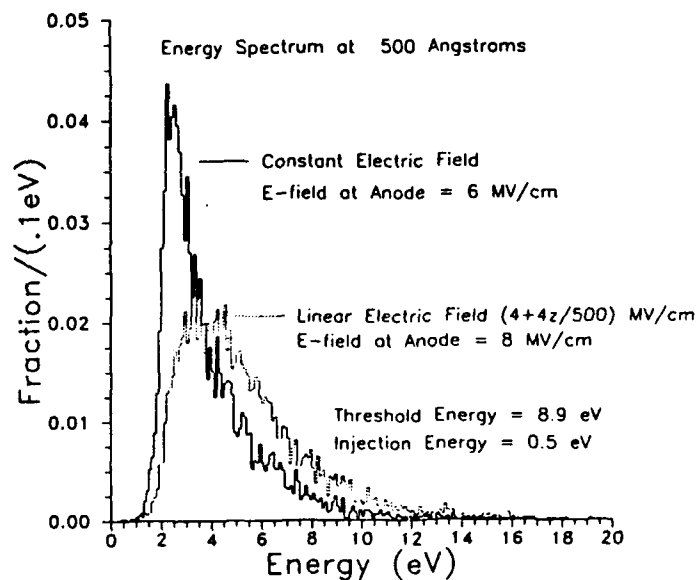


Fig. 25. Comparison of kinetic energy spectra with same average field values (6MV/cm) but differing anode fields, 6(-) and 8(---) MV/cm^[16].

2.1 Inelastic Electron-Electron Scatter in Conducting Materials

The differential cross section $\tau(E, \hbar\omega)$ for energy loss $\hbar\omega$ by an electron passing through a solid with kinetic energy $E (= \frac{1}{2}mv^2)$ is given by^[20]

$$\tau(E, \hbar\omega) = \frac{me^2}{\pi\hbar^2 E} \int_{k_-}^{k_+} \frac{dk}{k} \text{Im} \left[\frac{-1}{\epsilon(k, \omega)} \right], \quad (23)$$

where

E = kinetic energy of the incident charged particle (electron),
 \hbar = Planck's constant,
 $\hbar k$ = momentum transfer (incident electron to target electron),
 $\hbar\omega$ = energy transfer (incident electron to target electron),
 m = incident electron rest mass,
 e = electronic charge,
 $\epsilon(k, \omega)$ = exact dielectric function of the solid,
 and k_{\pm} correspond to the maximum (+) and minimum (-) allowed momentum transfer values;

$$k_{\pm} \equiv \frac{\sqrt{2m}}{\hbar} [\sqrt{E} \pm \sqrt{E - \hbar\omega}], \quad (24)$$

For conducting materials, Ritchie^[7] first proposed the use of the Lindhard^[23] form for $\epsilon(k, \omega)$, the dielectric response function for conduction band electrons, as follows:

$$\epsilon(k, \omega) = 1 + \left(\frac{\chi^2}{z^2} \right) [f_1(x, z) + if_2(x, z)], \quad (25)$$

where $\chi^2 = e^2 / \pi \hbar v_F$,
 $z = k / 2k_F$,
 $x = \hbar\omega / E_F$,
 E_F = Fermi energy of the scattering material,
 $v_F = (2 E_F / m)^{1/2}$ = velocity of electron with kinetic energy E_F ,
 $k_F = (2m E_F / \hbar^2)^{1/2}$ = wave vector corresponding to the Fermi momentum;

the functions f_1 and f_2 are given by

$$f_1(x, z) = \frac{1}{2} + \frac{1}{8z} \left\{ [1 - (z - x/4z)^2] \ln \left| \frac{z - x/4z + 1}{z - x/4z - 1} \right| + [1 - (z + x/4z)^2] \ln \left| \frac{z + x/4z + 1}{z + x/4z - 1} \right| \right\} \quad (26a)$$

$$f_2(x, z) = \begin{cases} \frac{\pi x}{8z} ; & z + x/4z < 1 \\ \frac{\pi}{8z} [1 - (z - x/4z)^2] ; & |z - x/4z| < 1 < z + x/4z \\ 0 ; & |z - x/4z| > 1 \end{cases} \quad (26b)$$

Eq. 23 may be rewritten as

$$\tau(E, \hbar\omega) = \frac{\chi^2}{\pi a_0 E} \int_{z_-}^{z_+} dz \frac{z f_2}{(z^2 + \chi^2 f_1)^2 + (\chi^2 f_2)^2}, \quad (27)$$

where, from Eq. 24,

$$z_{\pm} = \frac{1}{2} (\sqrt{x + 1} \pm 1). \quad (28)$$

In Eq. 28 we have assumed that the incident charged particle is an electron. This assumption will be carried through the remainder of this discussion. Thus, the constant outside the integral is written in terms of the Bohr radius $a_0 \equiv me^2 / \hbar^2$.

We evaluated the cross section function for ionization due to excitation of conduction band electrons in aluminum. It was more convenient to express the scattering cross section not as an explicit function of the incident electron energy, E , and energy transfer, $\hbar\omega$, but rather in terms of the dimensionless quantities ϵ (not to be

confused with the dielectric function) and x . The parameter x has been previously defined. The parameter ϵ is the incident electron energy (measured from the Fermi level) in units of the Fermi energy:

$$\epsilon \equiv (E - E_F)/E_F. \quad (29)$$

The cross section for electron-electron inelastic scatter is then given as

$$\tau_{ee}(\epsilon, x) = \frac{\chi^2 \Theta(\epsilon - x)}{\pi a_0 (1 + \epsilon)} \int_{z_-}^{z_+} dz \frac{z f_2}{(z^2 + \chi^2 f_1)^2 + (\chi^2 f_2)^2}, \quad (30)$$

where $\Theta(\epsilon - x)$ is the step function which insures that the incident electron energy remains above the Fermi level.

A consequence of expressing the cross section for electron-electron scatter as in Eq. 30 is that the quantity $(1 + \epsilon) \tau_{ee}(\epsilon, x)$ is independent of ϵ , except for the step function, and could be readily evaluated by numerical integration. We have evaluated this function for the range $0 \leq x \leq 7$. Our result, shown in Figure 26, agrees with that obtained by Tung and Ritchie^[20].

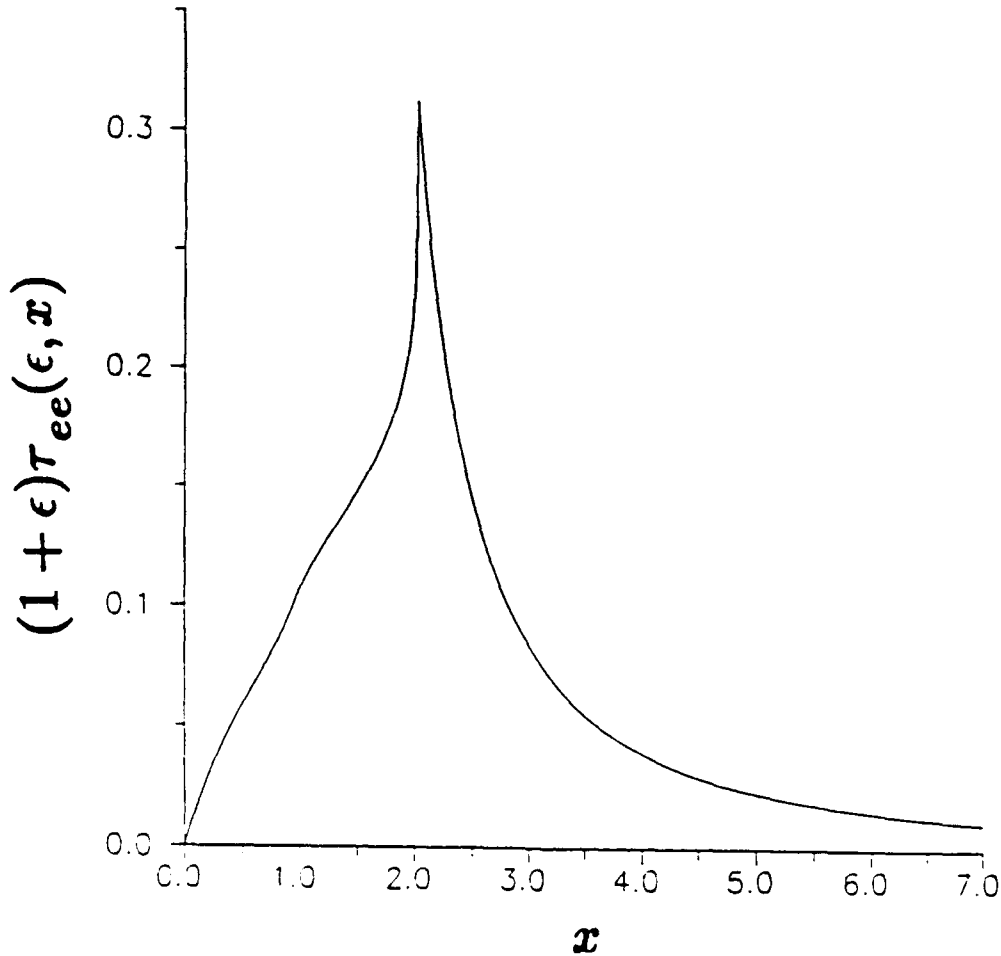


Fig. 26. Evaluation of normalized differential inverse mean free path $[(1 + \epsilon)\tau_{ee}(\epsilon, x)]$ for inelastic scatter with individual conduction band electrons in Al^[16].

The cross sections shown in Figure 26 were incorporated into a Monte Carlo code that we wrote for the purpose of "transporting" the electrons emerging from the SiO_2 layer through the aluminum layer. The trajectories of the primary electrons and the secondaries produced in the aluminum layer were traced, paying due attention to the multiple boundary crossings at the oxide-conductor interface. The electrons that re-entered the oxide layer were "banked", passed through the LOWEND code, and re-transported in the aluminum as many times as was necessary to produce a stable transmission spectrum from the aluminum. The resulting vacuum emission spectrum is shown in Figure 27. The integral transmission fraction was 0.064. This figure included energetic secondaries produced in the aluminum. As can be seen, there is no high energy tail as was experimentally observed^[18,19]. As stated in Ref. 16, there is reason to believe, based on discussions among researchers in this field, that the aluminum layers used in the experiments may have contained pinholes, and that the experimental data can be reproduced by linearly combining a proportionately small amount (fraction ~ 0.08) of the oxide anode spectrum with the aluminum emission spectrum.

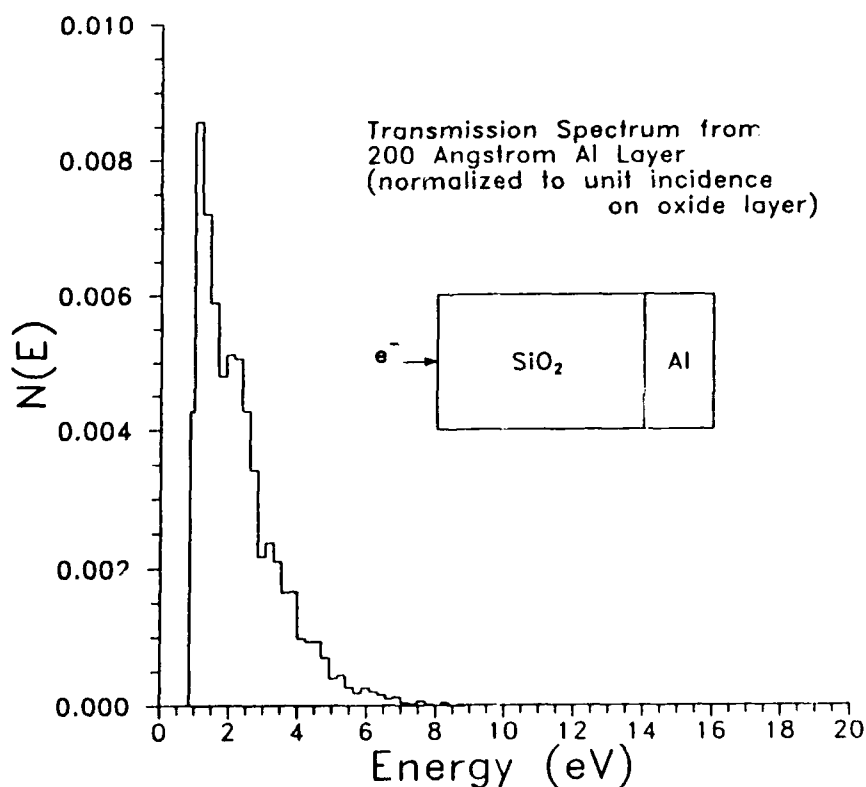


Fig. 27. Transmission spectrum through 200 Å Al anode adjoining 600 Å SiO_2 layer. Input spectrum, $\text{SiO}_2 \rightarrow \text{Al}$, is characteristic of an 8 MV/cm anode field^[16].

V. Monte Carlo Calculations of the Transport of MeV Electrons in Insulators

1. Introduction

The recent availability of experimental measurements of electric fields and charge distributions in such materials as polymethylmethacrylate (PMMA) by Zahn, Wright, Hikita, *et al.*^[24,25] has afforded an opportunity to study charge build-up in dielectric materials, an important factor in spacecraft charging. To study this and other data, and to perform numerical simulations of dielectric charging and breakdown, we wrote a Monte Carlo program ELMCF to calculate current, charge and energy deposition profiles in the presence of electric fields. Of existing electron Monte Carlo codes, the most widely used (and tested) is the ITS^[26] code series, which is incapable of handling problems involving applied electric fields. We were advised by one of the ITS authors that modification of this code to incorporate electric fields would probably destroy the code's utility. For this reason, we undertook to write our own ELMC, a simple Monte Carlo program that makes use of the same basic scattering algorithm as is used by the ITS series, the multiple scattering (condensed collision) formulation of Berger^[27,28]. After we were satisfied that ELMC performed correctly, we incorporated electric field effects into this program and named the expanded version ELMCF.

2. ELMC - Condensed Collision Electron Monte Carlo Code

The electron scattering model used in ELMC, is based on the screened-Rutherford cross section. Straggling and secondary electrons are not considered. Electron current, energy, charge deposition, transmission and reflection are calculated for a single material slab medium. The same algorithms as are found in the ITS series are used here to calculate the Legendre expansion coefficients of the screened-Rutherford cross section and the collision stopping power (including the energy-dependent density correction terms). The single collision cross section Legendre coefficients are then used to calculate the cumulative Goudsmit-Saunderson multiple-scattering angular distribution^[28]. The basic idea underlying the multiple-scattering angular distribution is that in the process of slowing down, the electron traverses a known path length segment, say Δs , for a given energy loss ΔE . Along this path length segment the electron undergoes many single collisions with other electrons in the scattering medium. Depending on the electron energy, a representative path length segment may account for as many as 300 to 400 collisions. For the energy range of interest we adopted Berger's algorithm^[28] of selecting N electron energy intervals where the upper bounds (E_n, E_{n+1}, \dots, E_N) of successive intervals ($\Delta E_n, \Delta E_{n+1}, \dots, \Delta E_N$), decreases by $2^{-1/8}$ ($= .9170$). With this as a guide, we then computed the Δs_n using the continuous slowing down approximation.

The remainder of the Monte Carlo program is a simple, standard trajectory analog code. The number of energy intervals, N , (or pathlength segments) depends on where one chooses the low energy cut-off, E_c , for the calculation. We chose to use the default value used in the ITS codes of $E_c = 0.05 E_0$, where E_0 is the source energy. This condition translate into 34 energy intervals, when the source energy was chosen as the highest energy value in the cross section table. In the ELMCF program, the number of energy intervals generally exceeded 34, since the presence of an electric field required allowance for the possibility of energy promotion above the source value.

The number of trajectory steps actually used in our Monte Carlo calculations was

approximately 3 times the number of energy intervals. In order to obtain an improved representative sampling of the multiple-scattering angular distribution, we split the Δs_n into equal size sub-steps within each ΔE_n , in this case 3 sub-steps of length $\Delta s_n/3$, and then sampling the multiple-scattering distribution 3 times as often. This is the same procedure as appears in the ITS codes. In the following four figures, we show some of the energy and charge deposition profile results obtained with ELMC, and compare them with results obtained with TIGER, the one-dimensional ITS Monte Carlo program. Both programs were run using 50000 case histories. The first two figures (Figs. 28 and 29) compare the energy and charge deposition profiles in PMMA for the case of a 0.4 MeV electron beam normally incident on a slab of thickness 0.14 g/cm², which corresponds to ~ 1.2 range units. The results are not identical, but track pretty well. The ITS codes contain a more complete cross section library that includes inelastic scatter. We believe that the differences are attributable to subtle differences in the evaluation of the multiple-scattering models. In the second two figures (Figs. 30 and 31) the energy and charge deposition profiles in aluminum are compared for a 5.0 MeV electron beam incident on a 3.2 g/cm² slab (~ 1.2 range units). As can be seen, the two Monte Carlo calculations are in good agreement.

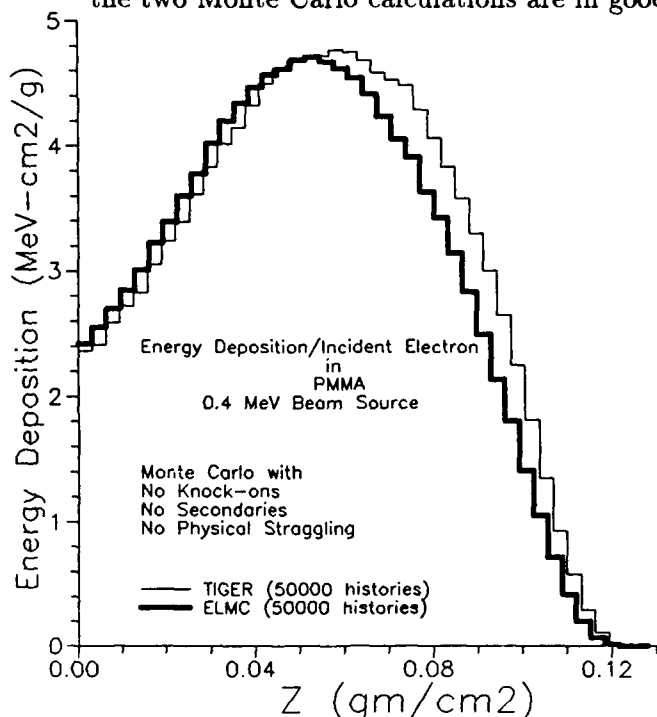


Fig. 28. Comparison of energy deposition profiles calculated by ITS^[26] and ELMC. 0.4 MeV normally incident electron beam in PMMA.

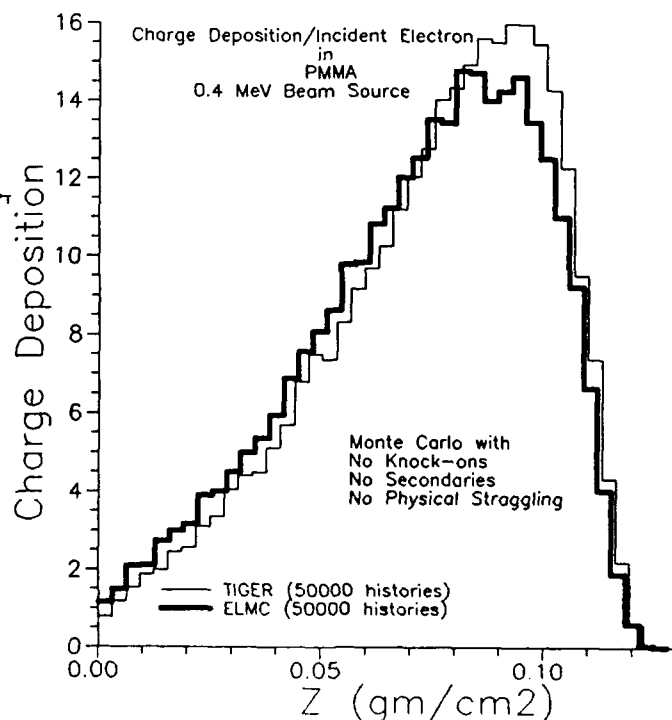


Fig. 29. Comparison of charge deposition profiles calculated by ITS^[26] and ELMC. 0.4 MeV normally incident electron beam in PMMA.

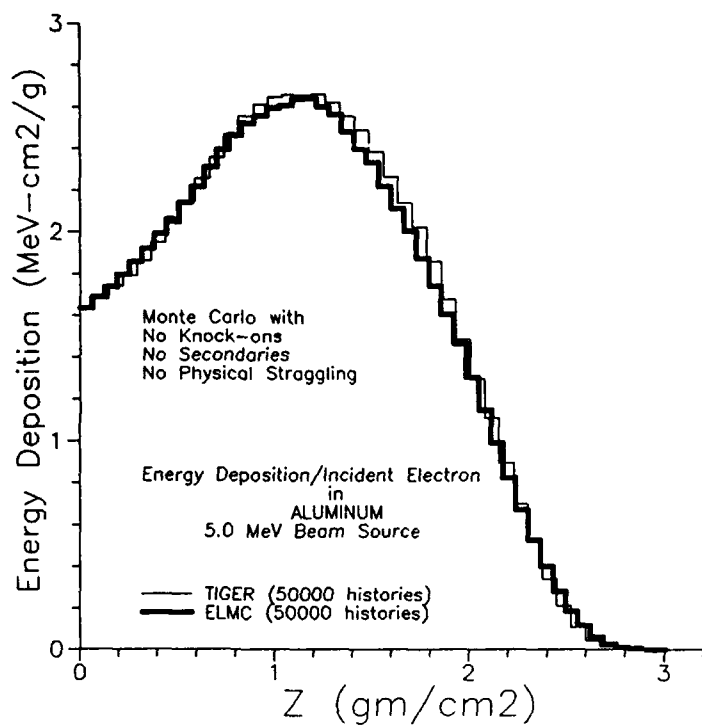


Fig. 30. Comparison of energy deposition profiles calculated by ITS^[26] and ELMC. 5.0 MeV normally incident electron beam in Al.

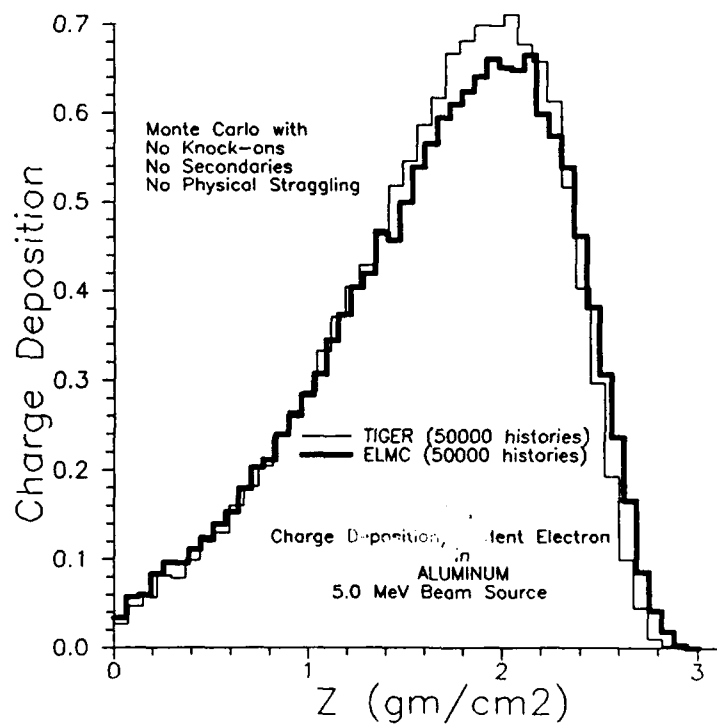


Fig. 31. Comparison of charge deposition profiles calculated by ITS^[26] and ELMC. 5.0 MeV normally incident electron beam in Al.

In Figure 32 we show current, energy and charge deposition profiles for one of the experimental configurations reported in Ref. 25, a 2.6 MeV electron beam normally incident on a PMMA slab of thickness 1.4 g/cm^2 . The electron beam is first diffused by 0.1 g/cm^2 PMMA before entering the 1.4 g/cm^2 slab. The attenuation accounts for the incident current having a value slightly less than unity. The histogram curves of Fig. 32 represent the first iteration (zero applied field) in a series of Monte Carlo calculations. Each subsequent iteration (Monte Carlo calculation) will be made using ELMCF with internal electric fields calculated from the current profile curve of its predecessor.

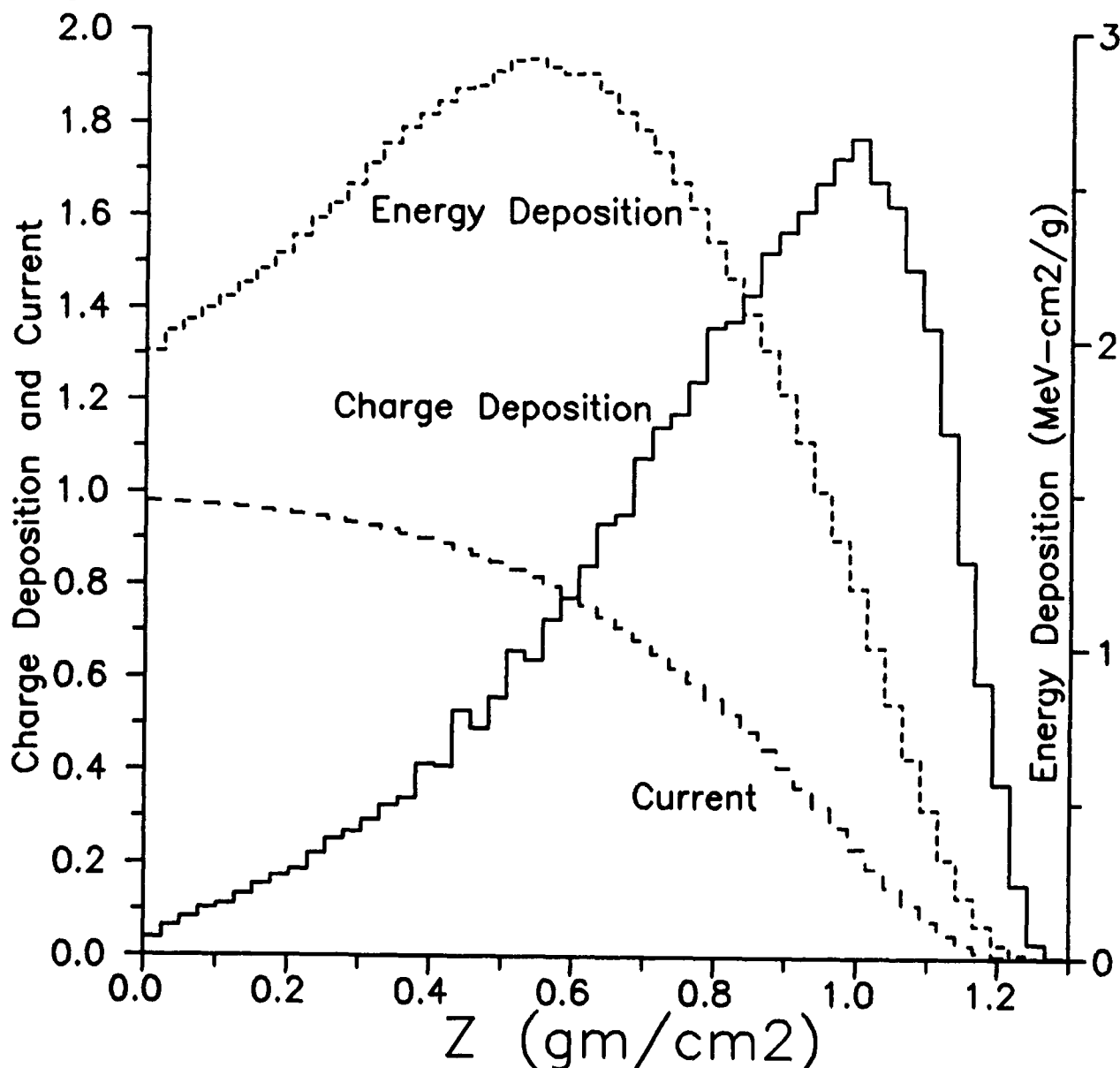


Fig. 32. Current, energy and charge deposition profiles for a 2.6 MeV electron beam normally incident on 1.4 g/cm^2 PMMA.^[25] The incident beam is diffused through 0.1 g/cm^2 PMMA prior to entry into slab.

We also compared results obtained with ELMC with energy and charge deposition profiles as calculated by our S_N discrete ordinates program, SNCODE. In the next two figures (Figs. 33 and 34) we compare the 0.4 MeV electron beam profiles as obtained by the two methods. The physical models used in both methods are based on the same screened-Rutherford scattering cross sections. ELMC incorporates these into the Goudsmit-Saunderson multiple-scattering model, while SNCODE employs the P-12 extended transport correction. The results obtained by the two methods converge as the number of energy groups (and the computational effort) is increased from 40 to 120. Depending on the problem parameters, the ELMC run time on a 386 PC for 50000 case histories is typically of the order of 1-2 hours.

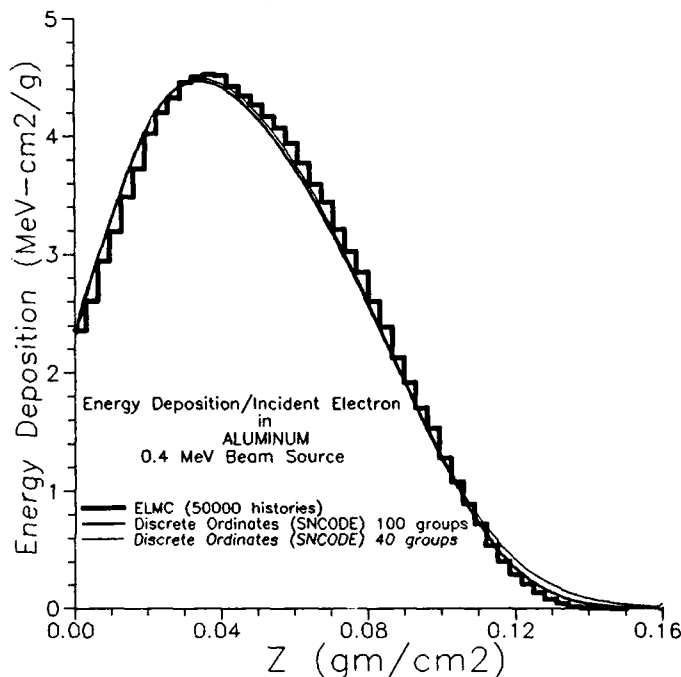


Fig. 33. Comparison of energy deposition profiles calculated by ELMC and SNCODE (100 and 40 groups). 0.4 MeV normally incident electron beam in Al.

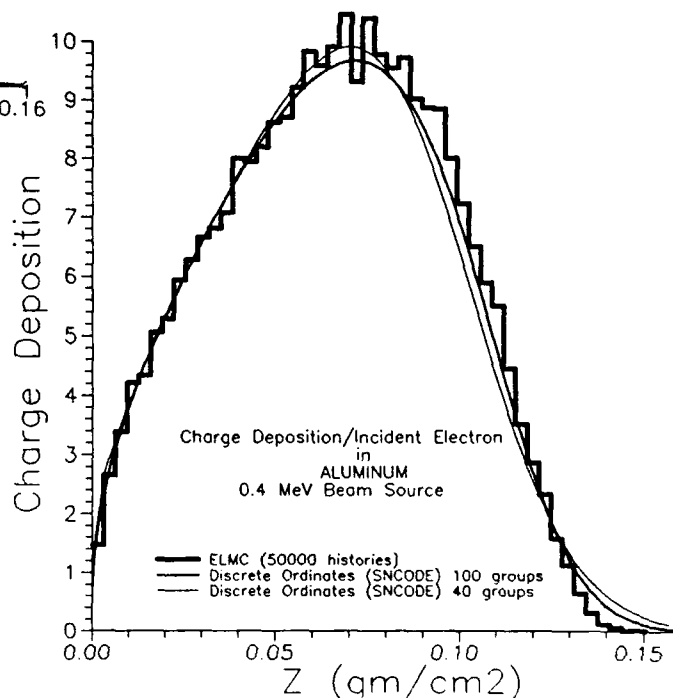


Fig. 34. Comparison of charge deposition profiles calculated by ELMC and SNCODE(100 and 40 groups). 0.4 MeV normally incident electron beam in Al.

3. ELMCF-Condensed Collision Electron Monte Carlo Code for Applied Electric Field Problems

Inclusion of electric field effects in our electron transport Monte Carlo calculations required modification of the penetration (PENET) and energy tally (SCORE) subroutines of ELMC. In the penetration routine, the principal modification was that of dividing the pathlength increment into fine sub-intervals $\delta s_n (= \Delta s_n / 15)$ and calculating the change in electron trajectory and energy within that sub-interval brought about by the acceleration or deceleration due to the presence of the electric field. By the use of sub-intervals, it was anticipated that each of these incremental changes would amount to a small perturbation in the overall trajectory and that their cumulative effect would be the smooth incorporation of energy and trajectory changes over a path length step Δs_n . The following two graphs (Figs. 35 and 36) illustrate the effects of uniform positively directed (along z) applied electric fields on energy and charge deposition profiles. The calculations were made for a 2.6 MeV electron beam normally incident on PMMA. There are four histograms in each graph, corresponding to $\mathcal{E}_z = 0.0, 0.5, 1.0, 1.5$ MV/cm. In the simulation of the experimental situation described in Ref. 25, the maximum field strength encountered is ~ 1.5 MV/cm and is in general not uniform across the slab. ELMCF has the capability to operate with spatially varying electric field \mathcal{E}_z .

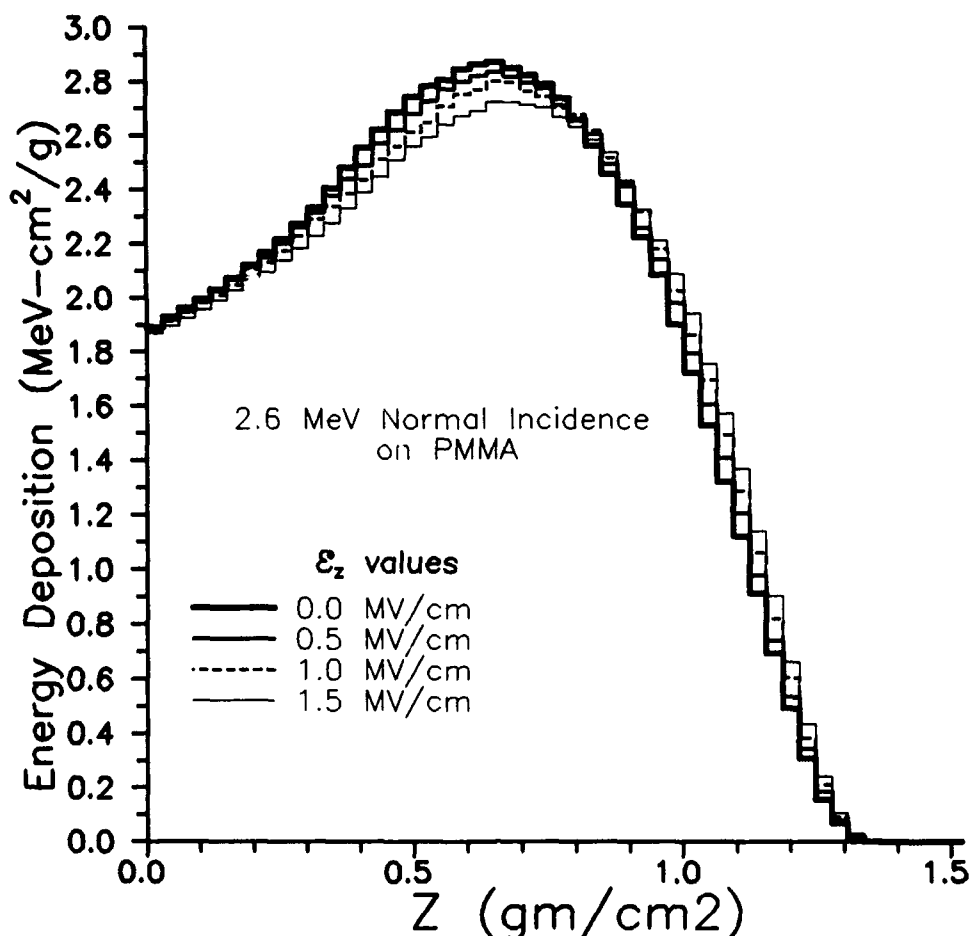


Fig. 35. Energy deposition profiles, as calculated by ELMCF, in PMMA in the presence of a positively directed constant electric field for a 2.6 MeV normally incident electron beam. Results for 4 field values are shown (0, 0.5, 1.0, 1.5 MV/cm).

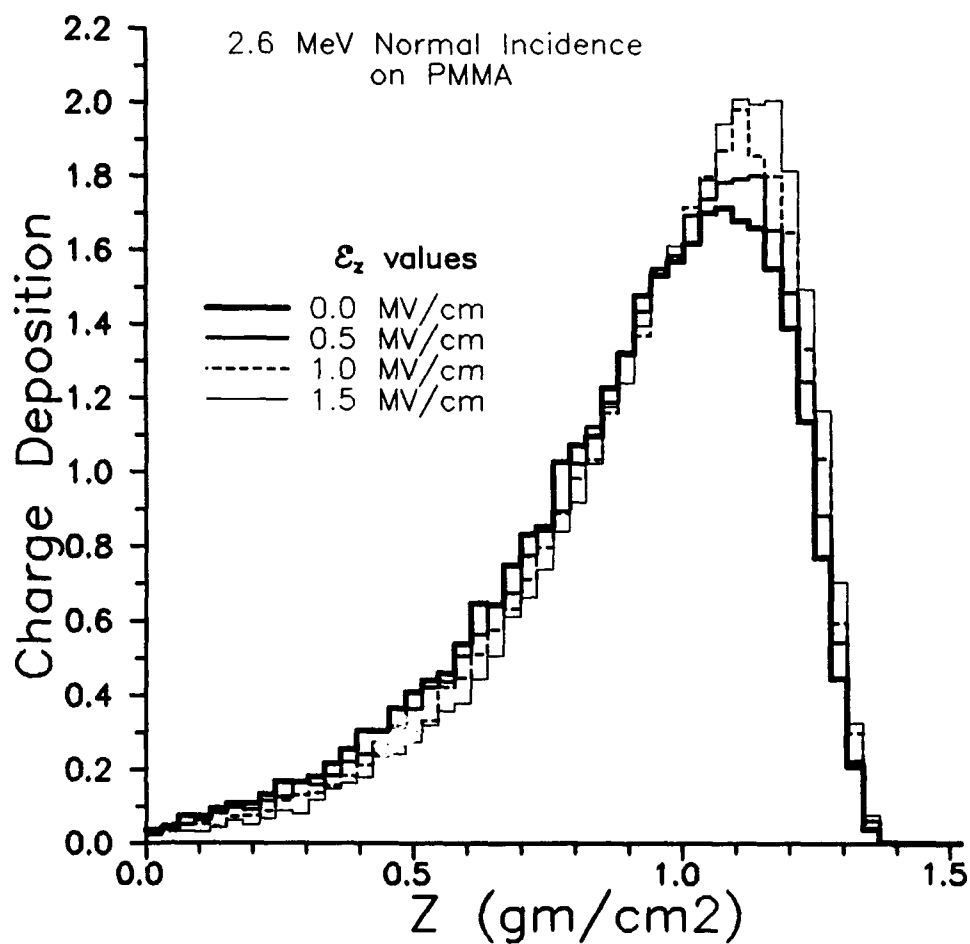


Fig. 36. Charge deposition profiles, as calculated by ELMCF, in PMMA in the presence of a positively directed constant electric field for a 2.6 MeV normally incident electron beam. Results for 4 field values are shown (0, 0.5, 1.0, 1.5 MV/cm).

VI. References

1. T. R. Hill, "ONETRAN": A Discrete Ordinates Finite Element Code for the Solution of the One-Dimensional Multigroup Transport Equation", LA-5990-MS, Los Alamos National Laboratory (1975).
2. S. Woolf, "Calculations of Electron and Photon Transport Between 1 MeV and 1 eV", Rome Laboratory Report RL-TR-91-289, November 1991.
3. B. R. Wienke, "ESN: One Dimensional Transport Module for Electrons", *J. Quant. Spect. Rad. Trans.*, **28**, 311 (1982).
4. S. Woolf and J. N. Bradford, "Discrete Ordinates Calculations of Low Energy Electron Transport in Silicon Dioxide In the Presence of an Electric Field", *Proc. ANS Top'l. Mtg. on Advances in Mathematics, Computations, and Reactor Physics*, ISBN-0-89448-161-4, 2, 7.2 1-1, Pittsburgh, PA (1991).
5. J. C. Ashley *et al.*, "Energy Loss and Scattering of Subexcitation Electrons in SiO₂", 10-th Annual Werner Brandt Conference on Penetration Phenomena, 1987.
6. S. Woolf and J. N. Bradford, "Monte Carlo Simulation and Analysis of Elastic and Inelastic Scattering of Electrons in Insulators", *IEEE Trans. Nucl. Sci.*, **NS-34**, No. 6, 1392 (December 1987).
7. R. Ritchie, *Phys. Rev.*, **114**, 644 (1959).
8. J. C. Ashley, V. Anderson, *IEEE Trans. Nucl. Sci.*, **NS-28**, 4132 (1981).
9. B. D. Ganapol, S. Woolf, and J. C. Garth, "Multigroup-S_n Benchmark Comparison for Electron Transport", *Proc. ANS Top'l. Mtg. on Advances in Mathematics, Computations, and Reactor Physics*, ISBN-0-89448-161-4, 5, 30.1 9-1, Pittsburgh, PA (1991).
10. J. E. Morel, *Nucl. Sci. Eng.*, **79**, 340 (1981).
11. S. Woolf, W. L. Filippone, B. D. Ganapol, and J. C. Garth, *Nucl. Sci. Eng.*, **92**, 110 (1986).
12. J. E. Morel, *Nucl. Sci. Eng.*, **71**, 64 (1979).
13. B. D. Ganapol, J. C. Garth, and S. Woolf, *Trans. Am. Nuc. Soc.*, **65**, 204 (1992).
14. B. D. Ganapol, "Application of the Numerical Laplace Transform Inversion to Neutron Transport Theory", *Transport Theory, Invariant Imbedding, and Integral Equations*, P. Nelson *et al.*, Eds., Marcel Dekker, Inc. (1989).
15. B. D. Ganapol, M. Alani, J. C. Garth, and S. Woolf, "Analytical Neutral Particle Benchmarks in Half-Space Geometry", Paper submitted to *Joint Int'l. Conf. on Math. Methods & Supercomputing in Nucl. Appl.*, Karlsruhe, (April 1993).
16. J. N. Bradford and S. Woolf, *Radiation Effects and Defects in Solids*, **117**, 227 (1991).

17. S.D. Brorson, et al., *J.Appl.Phys.* **58**, 1302(1985).
18. D.J. DiMaria, et al., *J.Appl.Phys.* **57**, 1214 (1985).
19. H. Fitting, A. Czarnowski, *Phys.Stat.Sol.* **93**, 385 (1986).
20. C. Tung, R. Ritchie, *Phys.Rev.B*, **16**, 4302 (1977).
21. J. Ashley, V. Anderson, *IEEE Trans. Nuc.Sci.*, **NS-28**, 4132 (1981).
22. C. Anderson, C. Crowell, *Phys. Rev. B* **5**, 2267 (1972).
23. J. Lindhard, "On the Properties of a Gas of Charged Particles", *Kgl. Danske Vid. Sels. Mat. Fys. Medd.*, **28**, No. 8 (1954).
24. M. Zahn, M. Hikita, K. A. Wright, C.M. Cooke and J. Brennan, *IEEE Trans. Elec. Insul.*, **EI-22**, No. 2, 181 (April 1987).
25. M. Hikita, M. Zahn, K. A. Wright, C.M. Cooke and J. Brennan, *IEEE Trans. Elec. Insul.*, **EI-23**, No. 5, 861 (October 1988).
26. J. A. Halbleib and T. A. Mehlhorn, "ITS: The Integrated TIGER Series of Coupled Electron/Photon Transport Codes", Sandia National Laboratories, Albuquerque, NM (November 1984).
27. M. J. Berger, "Monte Carlo Calculation of the Penetration and Diffusion of Fast Charged Particles", Methods in Computational Physics, B. Alder, S. Fernbach and M. Rotenburg, Eds., Academic Press, New York, 135 (1963).
28. M. J. Berger and R. Wang, "Multiple-Scattering Angular Deflections and Energy-Loss Straggling", Monte Carlo Transport of Electrons and Photons, T. M. Jenkins, W. R. Nelson and A. Rindi, Eds., Plenum Press, New York, 21 (1988).

**MISSION
OF
ROME LABORATORY**

Rome Laboratory plans and executes an interdisciplinary program in research, development, test, and technology transition in support of Air Force Command, Control, Communications and Intelligence (C³I) activities for all Air Force platforms. It also executes selected acquisition programs in several areas of expertise. Technical and engineering support within areas of competence is provided to ESD Program Offices (POs) and other ESD elements to perform effective acquisition of C³I systems. In addition, Rome Laboratory's technology supports other AFSC Product Divisions, the Air Force user community, and other DOD and non-DOD agencies. Rome Laboratory maintains technical competence and research programs in areas including, but not limited to, communications, command and control, battle management, intelligence information processing, computational sciences and software producibility, wide area surveillance/sensors, signal processing, solid state sciences, photonics, electromagnetic technology, superconductivity, and electronic reliability/maintainability and testability.